LLNL-JRNL-2003596

In situ deformation of antigorite-olivine two-phase mixtures: Implications for dynamics and seismic anisotropy in the mantle wedge

R Hurlow

December 2025

Earth and Planetary Science Letters

Disclaimer

This work performed under the auspices of the U.S. Department of Energy by Lawrence Livermore National Laboratory under Contract DE-AC52-07NA27344.

In-situ deformation of antigorite-olivine two-phase mixtures: implications for the dynamics and seismic anisotropy in the mantle wedge

Rose Hurlow[a, b#], Wenhao Su[c#], Wen-Yi Zhou[c], Feng Lin[d], Lowell Miyagi[d], Timothy Officer[e], Tony Yu[e], Yanbin Wang[e], Meiqian Wu[f], Qin Wang[f], Jin Zhang[a,c*]

a. Department of Earth and Planetary Sciences, University of New Mexico, Albuquerque, NM, 87131, USA
b. Lawrence Livermore National Lab, 7000 East Avenue, Livermore, CA, 94550, USA
c. Department Geology and Geophysics, Texas A&M University, College Station, TX, 77843, USA
d. Department of Geology and Geophysics, University of Utah, Salt Lake City, UT, 84112, USA
e. Center for Advanced Radiation Sources, The University of Chicago, Chicago, IL, 60439, USA
f. School of Earth Science and Engineering, Nanjing University, Nanjing, Jiangsu, 210023, CHINA
# These authors have equal contributions to this study; *corresponding author.

Abstract:

Subducting slabs release water from hydrous minerals, which reacts with the overlying mantle wedge, resulting in widespread serpentinization. Deformation of serpentinized mantle peridotite has been invoked to explain commonly observed seismic anisotropy in subduction zones. However, most previous deformation experiments have focused on single-phase mineral aggregates. The mechanical properties and deformation behaviors of multi-phase mixtures can significantly deviate from simple predictions based on volumetric proportions of individual minerals, especially when those minerals possess markedly different properties. Thus, in this study, we experimentally investigated deformation behaviors of two-phase mixtures composed of the most common anhydrous and hydrous minerals in the upper mantle: olivine and antigorite. We explored a range of volume proportions of these minerals under high pressure-temperature conditions (2.5-7.6 GPa, 673 K) and strain rates (from ~$1.0*10^{-5}$ to ~$1.0*10^{-4}$ s^{-1}). Deformation-induced crystallographic preferred orientation (CPO) of olivine and antigorite were measured using synchrotron X-ray diffraction (XRD) and were compared with Electron Backscatter Diffraction (EBSD) measurements of 2 selected from quenched run products. Elasto-Viscoplastic Self-Consistent (EVPSC) simulation was used to model lattice strain and CPO development to determine flow strength and deformation mechanisms. We found that the modeled stress on olivine based on EVPSC simulation increases with decreasing antigorite fraction and the structure of the two-phase mixture transitions from an interconnected weak layer (IWL) to a load-bearing framework (LBF). The CPO of olivine shifts from A- to C-type as the LBF forms, indicating a co-evolution of structure with CPO. The viscosity and strength of the two-phase mixtures increase as the antigorite fraction decreases. Additionally, the shear wave anisotropy of the deformed sample increases significantly with antigorite fraction. Pre-existing CPOs in the mixture promote the formation of the LBF. This study underscores the importance and feasibility of using multi-phase in situ experiments for better understanding of complicated geologic settings, such as mantle wedge.

Keywords:

Two-phase mixtures, Stress estimation, Crystallographic preferred orientation (CPO), Seismic anisotropy, Mantle wedge

1. Introduction

Mantle wedge is a unique section of the upper mantle above a subducting slab and below the overriding plate, extending from the forearc to the volcanic arc (Fig.1). This region undergoes complicated geological processes, including slab dehydration, partial melting, metasomatism, small- to middle-scale mantle convection, and delamination, all of which are crucial for understanding subduction zone dynamics. Small- to middle-scale mantle convection within the mantle wedge is closely tied to seismic anisotropy, particularly trench-parallel anisotropy in subduction zones, and plays an important role in volatile recycling in the Earth's interior (Kamiya and Kobayashi, 2000; van Keken et al., 2002; Long and van der Hilst, 2006; Wada et al., 2008; Wiens et al., 2008; Long and Wirth, 2013; Kenyon and Wada, 2022). Previous investigations attribute the observed strong seismic anisotropy to the CPOs of olivine and serpentine, with serpentine, particularly antigorite, being a major fluid alteration product in the deep mantle wedge (Guillot et al., 2015, Evans et al., 2013; Bezacier et al., 2013; Satta et al., 2022). Trench-parallel anisotropy in the mantle wedge is often associated with the alignment of antigorite's basal plane with the slab-wedge interface, B-type olivine CPO, or complicated 3D mantle flow fields, such as the trench-parallel flow beneath and above the slab (Long and Becker, 2010; Long and Wirth, 2013; Becker and Lebedev, 2021). In situ high-pressure-temperature deformation experiments (Zhang and Karato, 1995; Hilairet et al., 2007; 2012; Katayama et al., 2004; 2009; Katayama and Karato, 2006; Burnley, 2015; Burnley and Kaboli, 2019; Shao et al., 2021; Hilairet et al., 2024 etc.) and studies of exhumed naturally deformed serpentinized peridotites (Nishii et al., 2011; Shao et al., 2014; Soda and Wenk, 2014; Auzende et al., 2015; Morales et al., 2018; Horn et al., 2020; Liu et al., 2020; Hirauchi et al., 2021 etc.) have provided valuable insights into the deformation behaviors and CPO of antigorite and olivine in the mantle wedge.

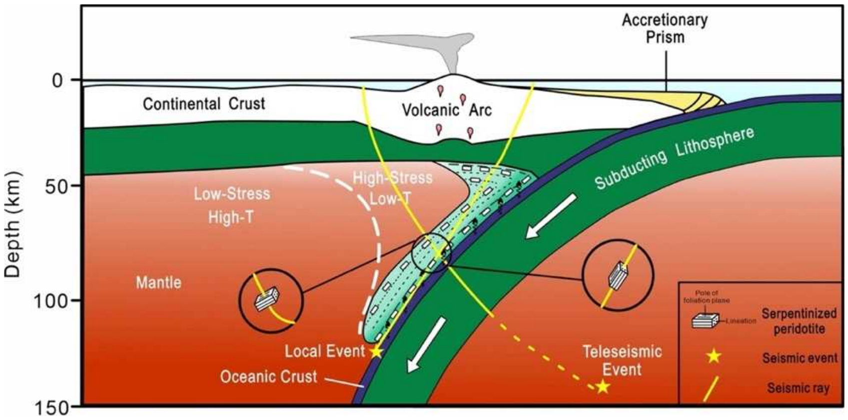

Fig. 1 Schematic diagram of the mantle wedge. The strains of the mantle wedge are higher in the area close to the slab and become lower where far away from the slab.

Understanding the deformation induced CPO of olivine and antigorite is essential for studying mantle wedge dynamics, as inferred from the shear wave splitting observations. Water plays a key role in the formation of mineral CPOs; for instance, olivine develops A- or D-type CPO under dry conditions and B, C, or E-type CPO under wet conditions (Jung and Karato, 2001). Further studies by Katayama and Karato (2006) and Jung et al. (2006, 2009a) found that olivine CPO development is also influenced by factors such as stress conditions and confining pressures. Development of antigorite's CPO is sensitive to deformation strain: the [100](001) and [010](100) CPO clearly show up when the shear strain (γ) exceeds 0.8 (Katayama et al. 2009; Hirauchi et al. 2010). Additionally, the deformation geometry (simple shear vs. axial shortening vs. pure shear) can also affect the symmetry of antigorite CPO (Padrón-Navarta et al. 2012). However, the exact activation conditions for these CPOs remain unclear.

Although studies of naturally deformed antigorite and olivine-bearing rocks have documented their textural relationships (e.g., Hirauchi et al., 2010; Jung et al., 2018; Liu et al., 2020; 2024), in-situ multi-phase deformation experiments are scarce (Ferrand. 2017; Ferrand et al. 2017; Hilairet et al. 2024). The deformation behavior of mineral mixtures is complex, as the rheology of individual minerals does not directly predict the aggregate's response. Handy (1990; 1994) defined two end-member multi-phase structures: a LBF structure and an IWL structure. In a LBF structure, stress is primarily borne by the structurally interconnected strong phase, whereas in an IWL structure, most of the strain is absorbed by the more abundant weaker phase. Intermediate structures of multi-phase aggregate between these two end members exist. However, studies on how these structures influence the mechanical behavior of mixtures remain limited.

Antigorite and olivine can exhibit substantial strength contrasts (Hilairet et al., 2007), suggesting that higher antigorite fraction could weaken the overall strength of the antigorite-olivine mixture. However, later studies (Chernak and Hirth, 2010; Proctor and Hirth, 2016) have challenged the estimation of antigorite's strength by Hilairet et al. (2007), citing low total strain (<15%) in their experiments. While typical rocks in hydrous mantle wedge contain more minerals than just olivine and serpentine (e.g., Grove et al., 2012), studying two-phase mixtures of antigorite and olivine provides valuable insights into the deformation behaviors of both strong (e.g., olivine, pyroxenes, etc.) and weak (e.g., antigorite, chlorite, etc.) phases in this dynamic region. A recent study by Hilairet et al. (2024) showed the strength of antigorite-olivine mixtures increases as antigorite volume fraction decreases, with 10 – 20 vol. % antigorite potentially changing the stress partitioning between antigorite and olivine, and thus the deformation behavior of the two-phase mixture. Ferrand et al. (2017), on the other hand, focused on the brittle deformation associated with antigorite dehydration under experimental conditions near its breakdown limit. However, the impact of antigorite fraction on the CPOs of olivine and antigorite, and their resulting seismic anisotropy remain unexplored. Moreover, fossil fabrics (or pre-existing CPOs of mineral grains) inherited from past geologic processes are known to influence rock deformation (e.g., Guo et al. 2024; Liu et al. 2016). The intrinsic elastic anisotropy of antigorite also drops quickly with pressure (Bezacier et al., 2013). To address these knowledge gaps, we performed in situ deformation experiments on antigorite-olivine two-phase mixtures with varying volume fractions at two pressure regimes (2.56 GPa-3.78 GPa and 6.44 GPa-7.09 GPa), at 673 K. The pressure and temperature conditions are within the stable field of antigorite (Ferrand et al., 2017; Wu et al., 2025); in this case, we analyzed CPO and lattice strain evolution during deformation without the influence of dehydration. In particular, we also deformed a starting sample with pre-existing CPOs for comparison. We then subsequently conducted EVPSC simulations to investigate stress-strain partitioning, fabric development, and aggregate strengths. Selected final run products were also analyzed using EBSD, and the results were combined with the EVPSC results to calculate the CPOs and seismic anisotropy of different run products. This study sheds light on how pressure, pre-existing CPOs, and the relative proportions of antigorite and olivine influence seismic observations in the mantle wedge.

2. Experiments

Natural samples of San Carlos olivine and antigorite from Estancia de La Virgen in the Motagua Mélange in Guatemala (American Museum of Natural History (AMNH), sample specimen MVJ87-6-2) were separately ground to powders with grain size varying between 5 and 50 μm. These powers were then mixed in varying volume proportions and sintered at 3 GPa and 400 K for 3 hours using the 2000-ton walker-type Multi Anvil Press at the High-Pressure Lab, University of New Mexico (UNM). The resulting rock cylinders (~4.5 mm in length and 1.6 mm in diameter) were then cut in half and lapped to final dimensions of 1.2 mm in length and 1.2 mm in diameter for synchrotron deformation experiments. During sintering, most of the olivine crystals remained randomly oriented while serpentine crystals developed a weak CPO with basal planes oriented at high angle to the load axis, as expected. Microstructure of the initial state will be shown later to compare with deformed samples. Among the 7 samples used in the deformation experiments, 6 were polished so antigorite's basal planes were oriented perpendicular to the axial compression direction of the D-DIA. The other sample, deformed in experimental run D2708, was polished to align the antigorite basal planes at ~45° to the axial compression direction, allowing investigation of deformation dependence on pre-existing CPOs (Fig. S1).

The deformation experiments were conducted using the D-DIA apparatus located at beamline 13-BM-D at GSECARS, APS, ANL (Yu et al., 2019). The polished cylinders were loaded into a cubic cell assembly (Fig. S1) designed for 4 mm truncation anvils. Table. 1

summarizes the experimental conditions for all experimental runs. The D-DIA setup enables control of differential stress via independent advancement of the top and bottom anvils, shortening the sample at a controlled temperature of 673 K under two hydrostatic pressure ranges: low-pressure (LP) runs between 2.56 GPa and 3.78 GPa, and high-pressure (HP) runs between 6.44 GPa and 7.09 GPa. Pressures and temperatures were measured by MgO pressure scale and pre-calibrated power-temperature curve, with estimated uncertainties of ~0.5 GPa for pressure and 10 % for temperature (Tange et al. 2009). X-ray radiographs were collected in situ to track axial strain, calculated as:

$$\varepsilon = (l - l_0)/l_0, \tag{1}$$

where l is the sample length during the deformation, and l_0 is the initial sample length, determined using Ni or Au foil placed at the top and bottom of the sample. Radiographs were acquired over 10s using a YAG scintillator and a charged coupled device (CCD). Radiograph collection alternated with a 2-D XRD imaging, taken every 400- 600 s. The synchrotron X-ray beam entered the sample through a gap between the anvils, allowing for a ~10° opening angle in 2θ. The experiments employed MAR-CCD and Pilatus detectors, provided full 360° coverage. The orientation of the detector with respect to the incoming beam as well as sample-detector distance were calibrated using CeO_2 and Al_2O_3 standards for each run.

Sample Name	Run Number	Antigorite -Olivine Volume Ratio	P (GPa)	Strain Rate (*10^{-5} s^{-1})	Olivine Estimated Stress (GPa)	Olivine EVPSC Stress (GPa)	Antigorite Estimated Stress (GPa)	Volume Averaged Mixtures Stress (GPa)	Maximum Strain (%)
Atg70/Ol30	D2608	70/30	6.77	2.77	2.37	2.27	1.27	1.60	23.1
	D2609	70/30	2.56	5.16	1.76	1.80	1.20	1.37	23.1
Atg50/Ol50	D2646	50/50	7.09	4.66	3.05	3.06	1.06	2.06	22.6
	D2647	50/50	3.78	3.28	2.68	2.66	1.06	1.87	20.4

Atg20/Ol80	D2705	20/80	6.44	3.64	3.44	3.40	1.78	3.24	21.6
	D2703	20/80	3.54	3.27	3.60	3.58	1.76	3.12	20.4
Atg50/Ol50*	D2708*	50/50	7.67	3.47	2.54	2.46	2.10	2.32	20.8

*Pre-sintered sample was rotated to align the antigorite basal planes at ~45° to the axial compression direction

Table 1 Summary of the experimental conditions of 7 runs

Selected samples were also examined using a JEOL JSM-6490 scanning electron microscope (SEM), EBSD measurements were completed with the conjunction of an Oxford Nordlys-S EBSD detector at the State Key Laboratory for Mineral Deposits Research, Nanjing University, China. The experimental setup and technical details are included in Supplementary Material Text S1.

3. Results

3.1 Stress estimation

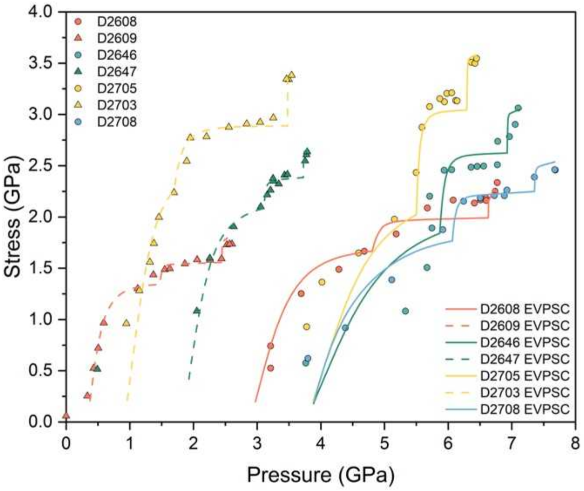

Fig. 2 Stress versus pressure plot for olivine in all experimental runs, modeled with EVPSC (lines) and calculated results (symbols). Solid lines and circles represent HP conditions (6.44 GPa-7.09 GPa), while dashed lines and triangles correspond to LP conditions (2.56 GPa-3.78 GPa). Estimated stress error calculated using Eq (2) is 0.25 GPa. The strain rates of all experimental runs are listed in Table 1.

We calculated differential stress (t) using the empirical equation in Singh et al. (1998):

$$t(hkl) = 6GQ(hkl), \tag{2}$$

where G is the shear modulus, $Q(hkl)$ is the lattice strain. G was calculated at the desired pressure and temperature condition for olivine and antigorite using single-crystal elasticity data from Zhang and Bass (2016) and Bezacier et al. (2013). Further details are provided in Supplementary Material Text S2 and Eq (S1-S3). Since only (001) and (102) lattice reflections were processable for the monoclinic antigorite, a full set of strained unit cell parameters could not be obtained, making EVPSC modeling unsuitable for evaluating antigorite's mechanical properties. However, for olivine, reflection of (021), (101), (002), and (130) are used to calculate the stress values, and compared to EVPSC modeling results (Wang et al., 2010) (Supplementary Material Text S3; Fig. S2, S4-S7; Eq S4-S5), showing close alignment between the two (Fig. 2). At both LP and HP conditions, the stress in olivine increases with decreasing antigorite fraction (Fig. 2), consistent with the progressive formation of LBF made of olivine, where stress is primarily borne by olivine.

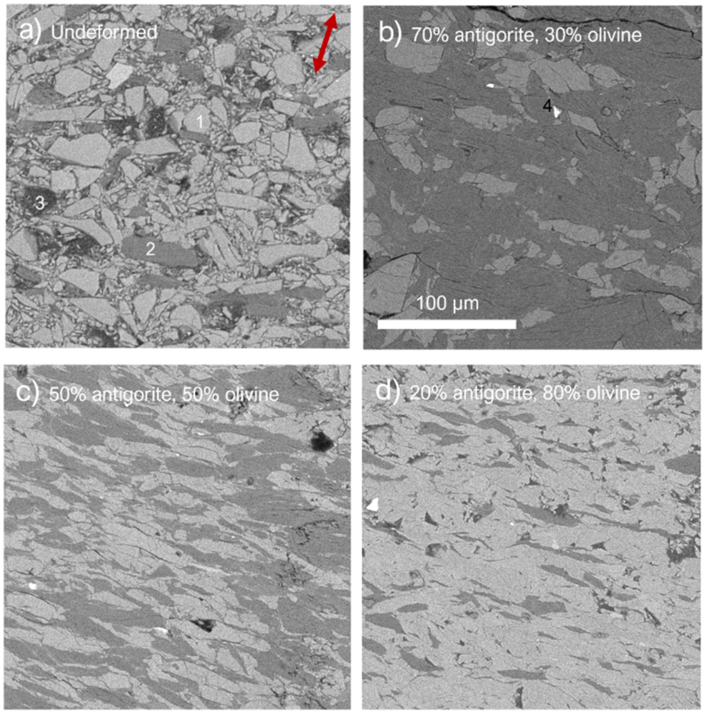

Fig. 3 SEM backscattered electron (BSE) images of undeformed and deformed samples. (a) undeformed sample with 20 vol.% antigorite and 80 vol.% olivine. (b) sample Atg70/Ol30 in run D2608 with 23.1% final strain. (c) sample Atg50/Ol50 in run D2646 with 22.6 % final strain. (d) sample Atg20/Ol80 in run D2703 with 20.4 % final strain. Numbers 1- 4 indicate: (1) olivine (2) antigorite (3) hole formed during polishing (4) magnetite. The red double-sided arrow in a) marks the axial compression direction (Z) for all samples.

BSE images (Fig. 3) of the deformed aggregates reveal consistent plastic deformation microstructures of antigorite with varying microstructures of olivine. No localized kinking of antigorite basal plane or comminution in the run products was observed. At 70 vol.% antigorite, the plastic strain is primarily accommodated by antigorite, forming an IWL microstructure around olivine clasts (Fig. 3b). The stress of olivine is low, similar to that of single-phase antigorite (Fig. 4). When the antigorite fraction decreases to 50 vol.%, a clast-matrix IWL framework forms, where both phases are interconnected (Fig. 3c). At 20 vol.% antigorite, the structure evolves into a LBF with interconnected olivine grains and scattered weak antigorite pockets (Fig. 3d). In this case, stress is predominantly supported by olivine. The modeled stress of olivine and the stress difference between olivine and antigorite both reach their greatest values of ~3.5 GPa and ~2 GPa, respectively (Fig. 4). Additionally, the modeled stress difference between olivine deformed at LP and HP conditions increases from 0.18 GPa at 20 vol.% antigorite, to 0.46 GPa at 70 vol.% antigorite (Fig. 4). This suggests that the isolated olivine grains surrounded by weak antigorite are more sensitive to external stress than those embedded in a stiff olivine framework. The modeled and extrapolated stresses for olivine in this study are consistent with results from Hilairet et al. (2024) at 1.89 GPa – 4.86 GPa, Hansen et al. (2019) at 7.0 GPa, and Long et al. (2011) at 4.3 GPa.

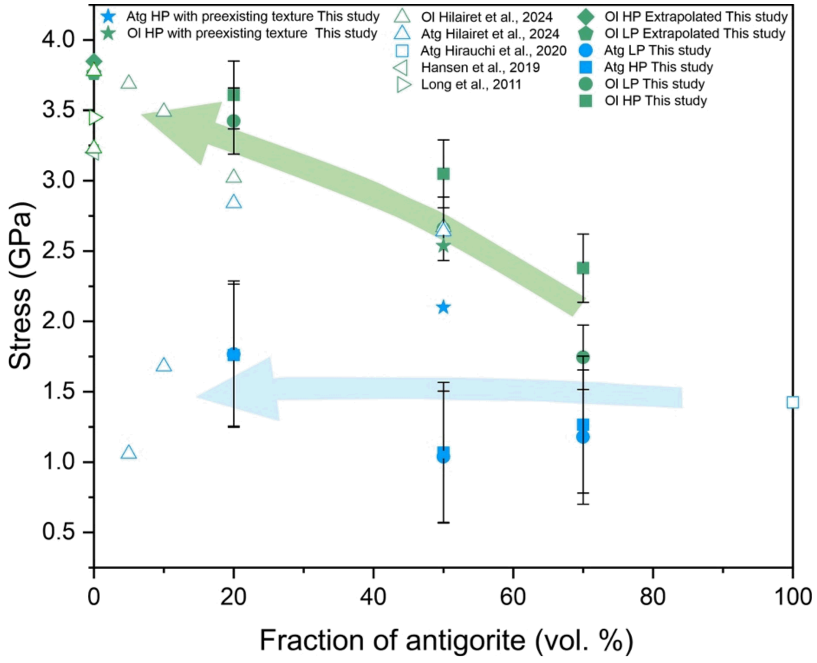

Fig. 4 Stress of the individual mineral phases in this study compared to previous single- or multi-phase deformation studies. The temperature and strange rate ranges in previous studies are 573 K – 673 K and $1*10^{-5}$ s^{-1} to $5*10^{-5}$ s^{-1}, consistent with this study. The pressure conditions are 1.89 GPa – 4.86 GPa (Hilairet et al., 2024), 7.0 GPa (Hansen et al., 2019), 4.3 GPa (Long et al., 2011), and 2 GPa (Hirauchi et al., 2020).

Interestingly, the calculated stress of antigorite appears lowest at 50 vol.%, and highest at 20 vol. % (Fig. 4). This trend contrasts with results from MgO (strong phase) - NaCl (weak phase) two-phase deformation experiments (Lin et al., 2019), where NaCl stress decreases as MgO fraction increases from 50 vol.% to 80 vol.%, likely caused by restricted NaCl percolation from obstruction by adjacent MgO grains. However, with only (001) and (210) peaks indexable, the estimated stress for the strongly anisotropic antigorite can be significantly biased (Amiguet et al. 2012). Given the large uncertainties associated with the calculated stress of antigorite, further studies with improved precision and more processable diffraction peaks are needed to confirm this variation trend. Additionally, pre-existing CPOs were found to increase the stress of antigorite while reduce the stress on olivine, suggesting that fossil fabrics play a crucial role not only in CPO development but also in stress partitioning within multi-phase aggregates.

3.2 CPO analysis

Synchrotron XRD data were analyzed using the software MAUD (Lutterotti et al., 1997), following the procedures outlined in Wenk et al. (2014). The CPOs of antigorite and olivine were refined using the E-WIMV algorithm, a modification of the original WIMV method (Matthies and Vinel, 1982) (Fig. S2). The fiber and non-fiber symmetry Orientation Distribution Function (ODF) files for both phases were exported from MAUD and smoothed using a 7.5° Gauss filter in the program BEARTEX (Wenk et al., 1998), which were then used to generate the Inverse Pole Figures (IPFs) and Pole Figures (PFs). The IPFs were then plotted in BEARTEX to infer the potential slip systems, while the PFs were plotted using the software MTEX (Bachmann et al., 2010) to compute the CPO strength indices (M-index and J-index, Table S1), as well as seismic anisotropy (Ben Ismail and Mainprice, 1998; Skemer et al., 2005). Although the total strain of each deformed sample varies, differences in CPO strength due to strain variations of less than 2.7% are likely negligible (Table 1). For instance, in run D2647, increasing strain from 15.4 % to 20.4 % only raised the M-index from 0.0202 to 0.0203, a minimal change. Therefore, we used the ODF files generated at the maximum final strain for CPO calculations.

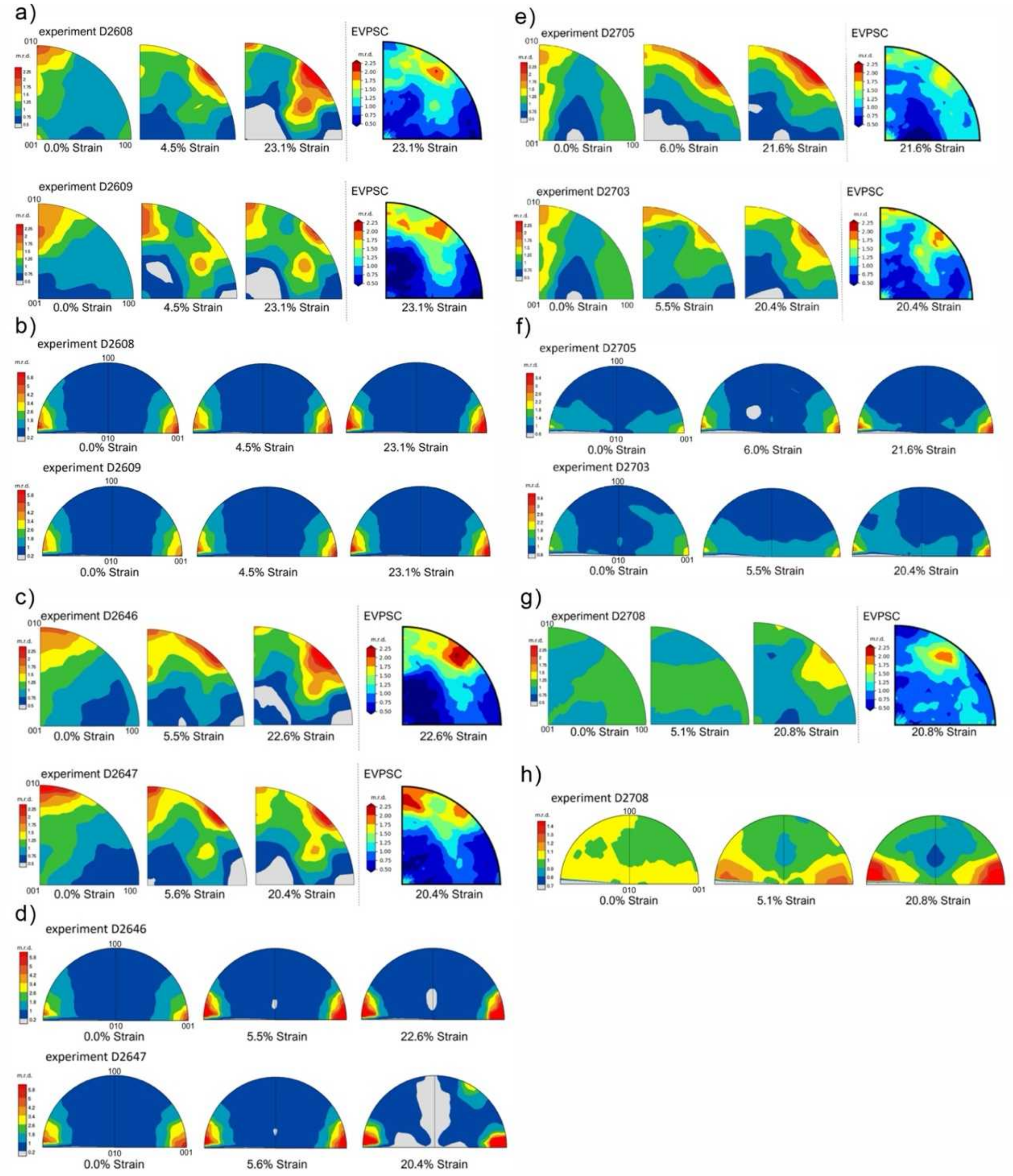

Fig.5 IPFs of experimental and modeled CPO of olivine and antigorite at different volume fractions: olivine in a) Atg70/Ol30, c) Atg50/Ol50, e) Atg20/Ol80, and g) Atg50/Ol50 with pre-existing CPOs; antigorite in b) Atg70/Ol30, d) Atg50/Ol50, f) Atg20/Ol80, and h) Atg50/Ol50 with pre-existing CPOs. Note the difference in color scales.

The IPFs (Fig. 5b, d, f, and h) show that the poles of antigorite basal plane (001) tend to align with the compressional direction (Z), suggesting the slip plane is (001) across all experimental runs. In contrast, the (010) and (110) poles of olivine concentrate along the Z direction (Fig. 5a, e, c, and g). For Atg20/Ol80, and Atg50/Ol50 with pre-existing CPOs, point maxima of (100) poles parallel to the Z direction can be observed except for the (010) and (110) poles (Fig. 5e, g), suggesting that the slip plane of olivine may change when the antigorite volume fraction decreases to 20% (D2703 and D2705) or when pre-existing CPOs are present (D2708). The slip system strengths might still be the same, but their activities can change under the influence of microstructures.

To further constrain the CPO formed in the final run products, we conducted EBSD experiments on samples Atg70/Ol30 and Atg50/Ol50 recovered from D-DIA runs D2608 and D2646 (Supplementary Material Text S1, Fig. S8). The EBSD results shown in Fig. S8 are highly consistent with the PFs of olivine shown in Fig. 6, with minor differences due to the 2D nature of EBSD analysis compared to 3D bulk sample analysis from XRD. Moreover, in D-DIA experiments, the one unique compression direction tends to orientate samples in the radial direction relative to the compression axis to form a radial symmetry (fiber symmetry). In this way, the PFs plotted using ODF data with non-fiber symmetry are likely to show artificial features in the plane perpendicular to the compressional direction (XY plane in Fig. 6 and Fig. 7) because of the limited data coverage and the resulting bias in ODF reconstruction. Thus, the X and Y directions mentioned in the following sections are not directly comparable to the real X and Y directions in pure shear and simple shear experiments, and the maxima and minima within the XY plane are likely artifacts.

As shown in Fig. 6, the CPOs of antigorite remain consistent across different compositions and pressures, with the (001) basal plane perpendicular to the Z direction. As expected, the EBSD and XRD results both suggest that the girdles of (100) and (010) poles are perpendicular to the Z direction, consistent with the fiber symmetry (Fig. 6; Fig. S8). Sample Ant50/Ol50 displays the strongest antigorite CPOs with the highest M-index and J-index values (Table S1). In comparison, the CPOs of the other two samples display weaker antigorite CPO and more dispersed poles concentrations in their PFs (Fig. 6). The CPO strength of antigorite is not very sensitive to pressure.

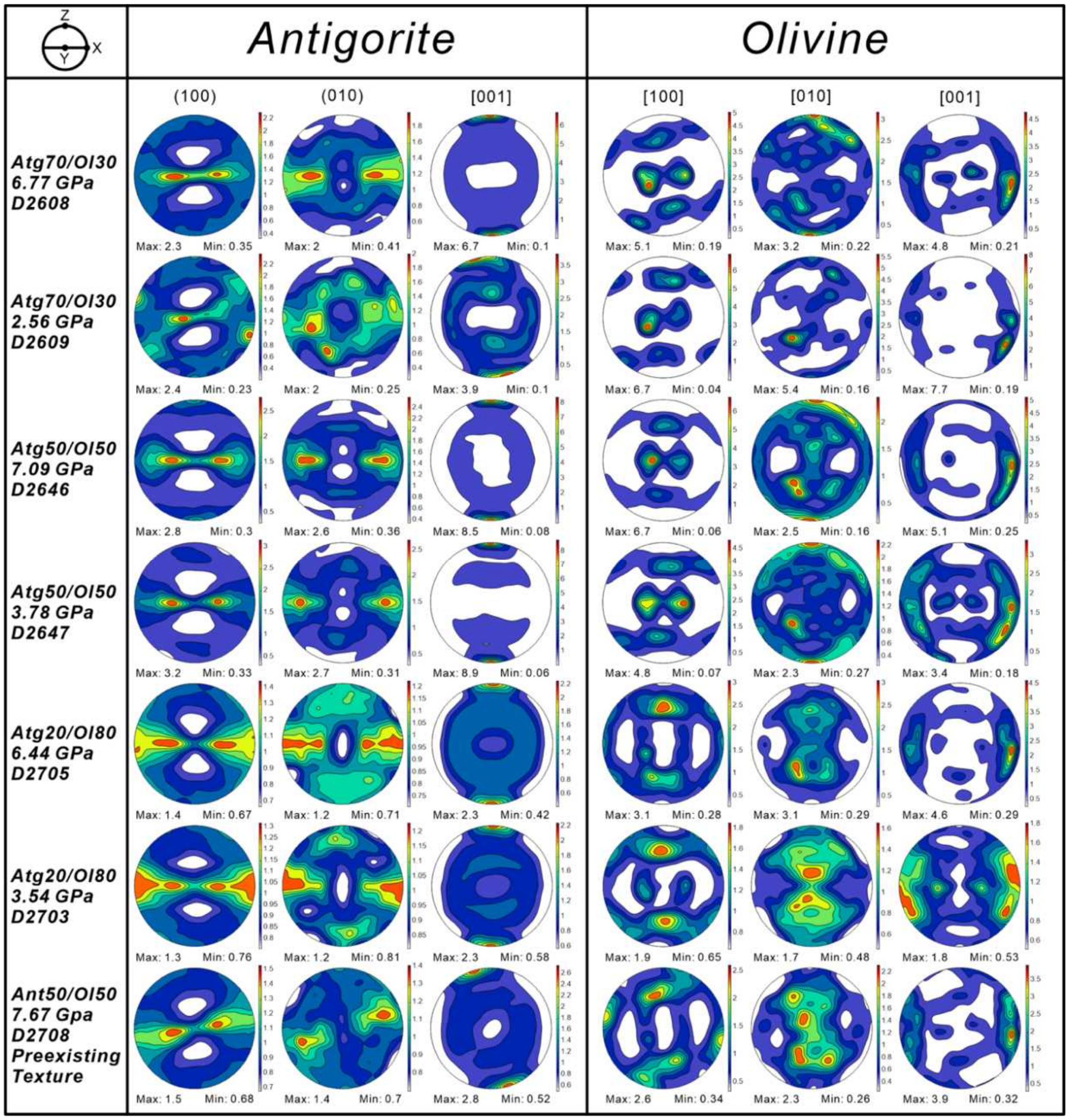

Fig. 6. Pole figures for samples with different antigorite-olivine volume fractions deformed under different conditions. Note, the CPOs implied in the X-Y plane are likely artifacts, thus are not comparable to the CPOs observed in previous pure shear and/or simple shear experiments.

The CPO strength of olivine is more sensitive to pressure than that of antigorite (Fig. S9b). For example, the M-index of olivine at ~7 GPa is higher than that at ~3 GPa when its volume exceeds 50% (Table S1). However, the opposite trend is observed when olivine constitutes only 30 vol% of the mixture (Table S1). Thus, when olivine forms an interconnected network, higher pressures promote the development of its CPO; conversely, when olivine grains are disconnected and surrounded by weaker antigorite, higher pressures reduce its CPO strength. In samples Atg70/Ol30 and Atg50/Ol50, the (010) poles align with the Z direction (Fig. 6), consistent with A or B-type olivine CPO. In contrast, most of the (100) poles of Atg20/Ol80 are parallel to the Z direction, which indicates the development of C-type olivine CPO. It is also noted that the gradual transition from A- or B-type to C-type olivine CPO with decreasing antigorite fraction is particularly evident from the progressive shift of (010) poles in the PFs (Fig. 6, Fig. S8).

To investigate the potential effect of pre-existing CPOs, we conducted experimental run D2708, where the weakly oriented basal planes of antigorite in Atg50/Ol50 were positioned at ~45° to the axial compression direction Z. The resulting CPO pattern of the antigorite showed slight rotation to the same sample deformed in runs D2646 and D2647, suggesting that pre-existing CPOs of antigorite can be easily overprinted by subsequent deformation under natural mantle wedge conditions. In contrast, the olivine CPO from run 2708 is identical to that of sample Atg20/Ol80, showing C-type CPO, whereas run 2646 for sample Atg50/Ol50 displays A- or B-type CPO. This suggests that pre-existing CPOs influences the development of olivine CPO in antigorite-olivine mixtures. The pre-existing antigorite CPOs applied in this study intersects the X and Z directions at about 45°, a geometry similar to that likely formed near the slab-mantle interface, influenced by corner flow (Kneller et al., 2008, Fig. 1). As expected, the strength of olivine CPO (e.g., M-index) (Fig. S9b) of Atg50/Ol50 in run D2708 (0.022) is weaker compared to run D2646 (0.0365) due to the presence of pre-existing CPOs. However, subsequent continuous deformation can erase these CPOs, leading to an eventual increase in CPO strength.

3.3 Seismic anisotropy calculation

Seismic anisotropy of deformed multi-phase aggregates can be calculated based on the single-crystal elastic moduli, volumetric fraction of minerals, and experimentally determined CPOs. The pressure and temperature-dependent single-crystal elastic moduli of antigorite and olivine were obtained from Satta et al. (2022) and Zhang and Bass (2016), with the temperature effect on antigorite neglected due to a lack of experimentally determined high-pressure-temperature single-crystal elasticity data. Again, due to deformation geometry and the potentially biased XRD data coverage, all features displayed in the XY plane need to be viewed with caution since artifacts can be introduced during the reconstruction of ODF.

In deformed two-phase mixtures without pre-existing CPOs, the compressional wave velocity anisotropy (AVp) and maximum shear wave velocity anisotropy (AVs) of antigorite range from 2.1% to 7.2% and 2.7% to 10.9%, respectively (Fig. 7; Fig. 9a). In comparison, olivine exhibits markedly lower AVp (1.1% - 3.9%) and AVs (0.9% - 3%) values (Fig. 7; Fig. 9b). Deformed Atg50/Ol50 shows the highest AVp and AVs for antigorite, consistent with the observed CPO strength. The minimum Vp direction of antigorite remains aligned with the Z direction (Fig. 7, Fig. S10), while the maximum AVs direction of antigorite are always within the XY plane (Fig. 7, Fig. S10).

For olivine, in the HP runs, Atg50/Ol50 shows the highest AVp and AVs (Fig. 9b). However, in the LP runs, Atg50/Ol70 and Atg70/Ol30 exhibits highest AVp and AVs values, repectively (Fig. 7; Fig. 9b). A significant change in the anisotropy pattern occurs when olivine fraction reaches 80 vol.%, corresponding to a transition from A- or B-type to C-olivine CPO. Indicating the anisotropy direction of olivine aggregates of the two-phase mixture is more sensitive to the antigorite fraction. The maximum AVs direction is along Z direction for sample Atg70/Ol30 and Atg50/Ol50, while the minimum AVs direction is parallel to the Z direction when the antigorite fraction decreases to 20 vol.% (Fig. 7).

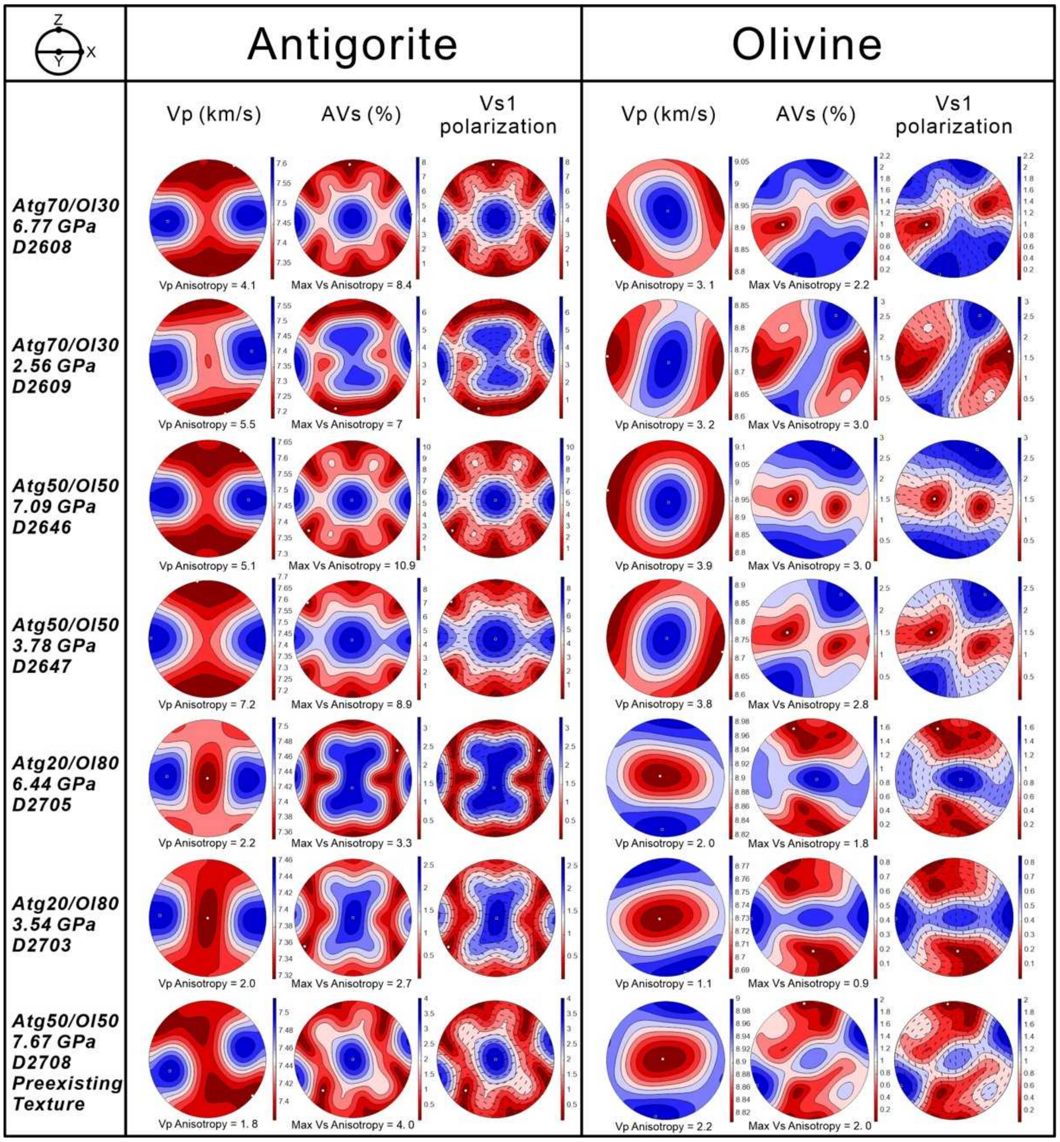

Fig. 7 Calculated anisotropy for antigorite and olivine in different experimental runs. Note, the anisotropy pattern displayed in the XY plane are likely artifacts.

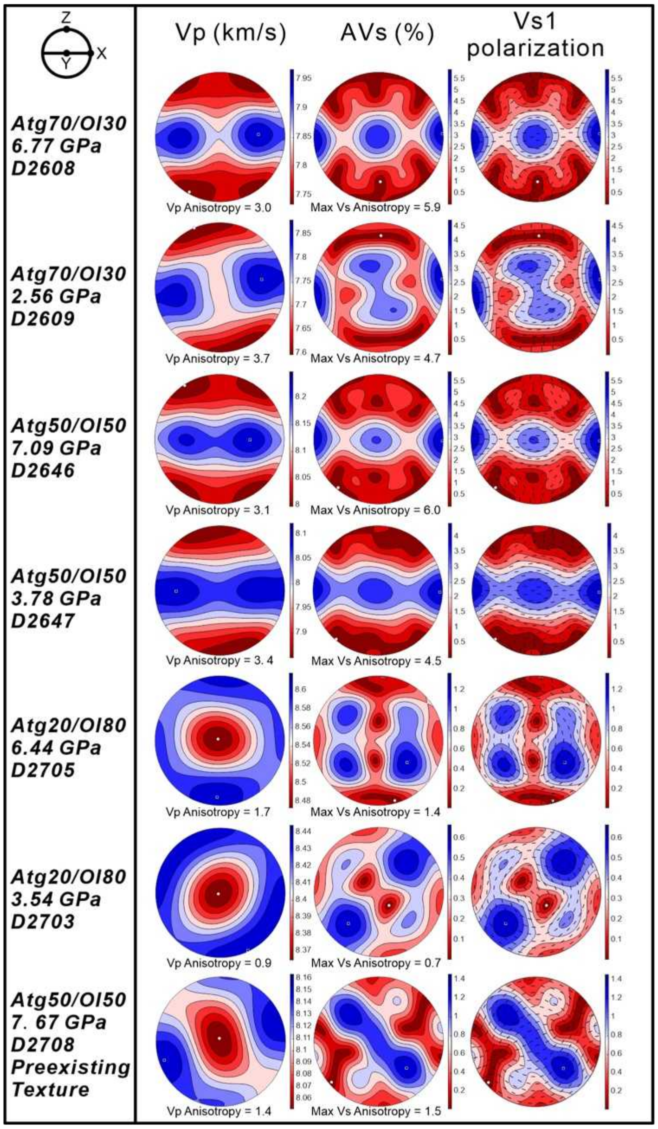

Fig. 8 Calculated anisotropy for antigorite-olivine two-phase mixtures in different experimental runs. Note, the anisotropy pattern displayed in the XY plane are likely artifacts.

The maximum AVp and AVs for the Atg50/Ol50 sample with pre-existing CPO, deformed in run D2708, are 1.4% and 1.5%, respectively (Fig. 8), markedly lower than sample Atg50/Ol50 without pre-existing CPO deformed in run D2646. The formation of C-type olivine CPO leads to a similar seismic anisotropy pattern comparable to that of sample Atg20/Ol80. The pre-existing CPO have not been completely overprinted yet in run D2708, thus it is difficult to estimate final seismic anisotropy upon further deformation. Future time-dependent studies at higher strains are needed.

The anisotropy values obtained in this study are lower than previous studies (Katayama et al., 2009; Hirauchi et al., 2010; Katayama and Karato. 2006; Jung et al. 2006; Ohuchi et al., 2012; Jung, 2011; Liu et al., 2020), likely due to differences in deformation geometry and total shear strain. The axial shortening D-DIA experiments conducted in this study are close to axial compression, and with smaller strains (< 50 %; e.g., Hirauchi et al., 2020; Shao et al., 2021) compared to those achieved in simple shear deformation experiments (as high as 478 %, Shao et al., 2021). Previous studies on single-phase antigorite (Katayama et al., 2009, Fig. 9a) or olivine (Ohuchi et al., 2012, Fig. 9b) reported shear strains exceeding 0.8 and 0.5, respectively. The shear strains reached in this study are likely significantly lower than in previous studies. Moreover, unlike simple shear, axial compression imposes strain along one unique principal compression direction, which likely results in weaker seismic anisotropy at comparable strain levels, as shown in Fig. 9.

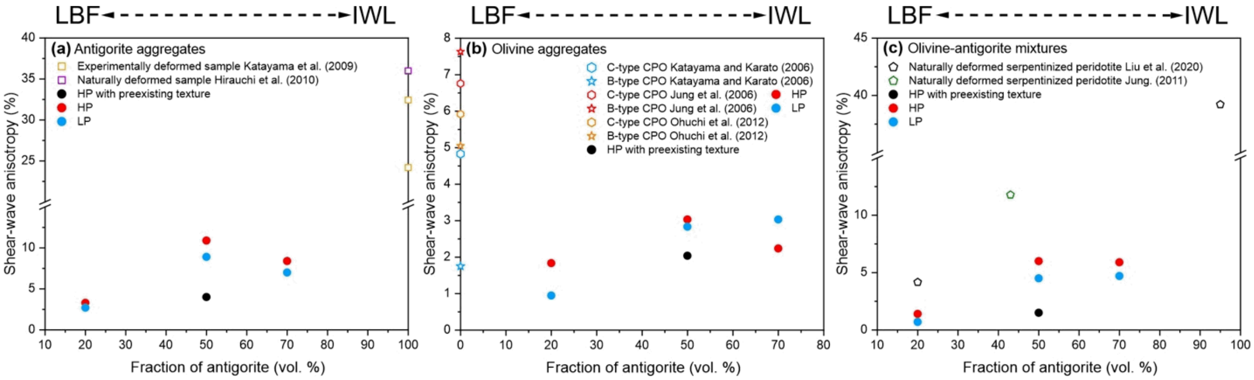

Fig. 9 Shear-wave anisotropy of (a) antigorite, (b) olivine, and (c) antigorite-olivine mixtures versus antigorite fractions compared with previous studies on experimentally deformed single-phase aggregates or naturally deformed serpentinized peridotites.

In conclusion, the anisotropy of the deformed antigorite-olivine two-phase mixtures depends on the single-crystal anisotropy, CPO strength, and volume fraction of each phase. As shown in Figs. 7 and 8, antigorite is the primary anisotropy contributor in Atg70/Ol30 and

Atg50/Ol50, while olivine plays a more important role in sample Atg20/Ol80. Pre-existing CPOs can also influence anisotropy, though their time-dependent effects require future studies.

4. Discussions

4.1 Brittle and ductile deformation of antigorite

Hilairet et al. (2007) found antigorite to be significantly weaker based on D-DIA experiments at 1-4 GPa and 473-773 K. This conclusion has been challenged by Chernak and Hirth (2010), who argued that < 15% axial strain could be insufficient to initiate localization, thus preventing the attainment of steady-state ductile flow. Previous studies also documented brittle and semi-brittle deformation of antigorite (Chernak and Hirth, 2010; Proctor and Hirth, 2016; Hirauchi et al., 2020; Shao et al., 2021; Jung et al., 2009b). Pressure promotes the brittle to ductile transition of antigorite (Escatin et al., 1997; Shao et al., 2021), whereas temperature can induce the reverse transition from ductile to brittle deformation, as internal friction decreases near antigorite's breakdown temperature (Proctor and Hirt, 2016; Hirauchi et al., 2020). Similar transitions have been observed in gypsum (Brantut et al., 2011) and talc (Escartin et al., 2008). An alternative explanation involves the formation of a new talc-like phase at the transition temperature (~723–773 K) (Gasc et al., 2017). Additionally, strain rate plays a critical role. Burdette and Hirth (2022) suggested that low strain rates (10^{-9} to 10^{-4} s^{-1}) can promote crystal plasticity and distributed deformation (ductile deformation), hindering localization. In this study, although the strain rate is relatively high (~$1.0*10^{-5}$ to ~$1.0*10^{-4}$ s^{-1}), the temperature of 673 K is below the ductile to brittle transition temperature of 723–773 K. The total strains of our experimental runs (20 % - 25 %) exceed the minimum localization strain suggested by Chernak and Hirth (2010). While the evident CPO of antigorite observed in this study is likely caused by ductile deformation, brittle deformation may still play a role. Hansen et al. (2020) demonstrated that antigorite CPO can form through progressive rotation of antigorite blades sliding along the basal plane without dislocation activity. Therefore, we suggest that antigorite deformation in this study is primarily ductile, especially considering the much higher pressure conditions (6.44 - 7.67 GPa) in the HP runs reached in this study compared to previous studies (Table S2). A potential contribution from semi-brittle deformation is possible for the LP (2.56 – 3.78 GPa) experimental runs in this study.

4.2 Deformation mechanism of antigorite

The CPO of antigorite has garnered lots of attention due to its potential to explain the trench-parallel anisotropy widely observed in subduction zones (e.g., Katayama et al., 2009; Bezacier et al., 2010; 2013; Jung et al., 2011). The dominant antigorite CPO slip systems identified in laboratory experiments and field samples are (001)[100] (Katayama et al., 2009; Bezacier et al., 2010) and (001)[010] (Hirauchi et al., 2010; Jung et al., 2011; Nishii et al., 2011; Soda and Takagi, 2010), although other types of CPO have been reported (e.g., Soda and Takagi, 2010; Jung et al., 2011; Nishii et al., 2011; Horn et al., 2020). Ji et al. (2013) proposed three end-member types of antigorite [001] axes CPO based on the Flinn diagram; the L-, LS-, and S-type correspond to the constructional, plane, and flattening strain, respectively. Liu et al. (2020) further classified antigorite CPOs into four categories: LS-a-type and LS-b-type with (001)[100] and (001)[010] slip systems, respectively; S-type shows girdles of both (100) and (010) poles parallel to the lineation; and finally L-type with (010) poles parallel to lineation and [001] girdle perpendicular to foliation. However, L-type CPO cannot be explained by the 4 slip systems considered by Padrón-Navarta et al. (2012): (001)[100], (001)[010], (001)<110>, and {110}[001]. Therefore, other factors may contribute to the formation of L-type CPO of antigorite in nature, which need further investigations. The antigorite CPO in this study shows [001] axes parallel to the compression direction Z, and both the (100) and (010) poles align within the XY plane, where we do not have date coverage. Therefore, although the specific type of CPO cannot be able to determine, the L-type can be rule out, since there is no maxima of (100) and (010) poles in the Z direction based on both XRD and EBSD results (Fig. 5; 6).

Katayama et al. (2009) found the CPO of antigorite depend on shear strain, which can explain the different CPOs observed in naturally deformed massive-type and schistose-type serpentine samples (Hirauchi et al. 2010). Padrón-Navarta et al. (2012) and Ji et al. (2013) proposed that the activation of different slip systems of antigorite depends on deformation regime or strain geometry (simple shear/axial shortening/transgressions/transtension; constructional/plane/flattening strain), with axial shortening and flattening strain promoting a strong S-type CPO. In this study, which utilizes axial compression, while shear strain cannot be ubiquitously determined due to the axial shortening geometry, the CPO patterns are not significantly affected by deformation regimes or total strain. Moreover, the pressure, stress, and pre-existing CPOs do not appear to be dominant factors, as antigorite CPOs formed under different pressure conditions show minimal variation. Although we cannot completely rule out the effect of stress on the antigorite CPO type as the range of estimated antigorite stress is limited (Fig. 4), the antigorite CPO type is likely insensitive to stress.

4.3 Transition of olivine CPO and the two-phase mixture framework

Mantle serpentinization occurs when hydrous fluids released by slab dehydration react with upper mantle rocks enriched in olivine, a strongly anisotropic mineral. As the most abundant mineral in the Earth's upper mantle, the deformation of olivine has been extensively studied as a function of pressure, temperature, and hydration levels (e.g., Zhang and Karato, 1995; Jung and Karato. 2001; Jung et al. 2006; 2009a; Katayama and Karato, 2006; Ohuchi et al., 2012; 2013). While the A-type CPO, activated by (010)[100] slip system, is considered the most common fabric in the upper mantle, other types of CPO can also develop under different conditions. Like A-type CPO, D-type CPO forms in dry olivine (water content < 200 ppm Si/H), but under higher stress (Bystricky et al., 2000). In hydrous olivine, B-type CPO develops under high stress with water content in olivine ranges from 200 to 1200 ppm H/Si, whereas C- and E-type CPOs are usually found in deformed olivine aggregates with > 700 ppm H/Si and 200 – 700 ppm H/Si contents but with lower stress (Jung and Karato. 2001). Moreover, at pressures exceeding 7 GPa, A-type CPO can still develop in olivine aggregates with extremely high water content (> 2130 ppm H/Si, Ohuchi and Irifune. 2013).

In this study, we observed a transition from A- or B-type to C-type olivine CPO when the antigorite fraction decreased to 20%. This result is unexpected, since the B- and C- type olivine CPO is favored for hydrous olivine, whereas San Carlos olivine used in this study are known to be dry (e.g., Mackwell et al., 1985; Zhang et al. 2019; Kumamoto et al., 2024). Although antigorite is a representative hydrous mineral in the mantle wedge, the experimental temperature (673 K) in this study falls within its stability field (Ferrand et al., 2017; Wu et al., 2025), thus dehydration is unlikely. In the meanwhile, Hilairet et al. (2024) reported the development of C-type olivine CPO in a sample containing 20 vol. % antigorite and 80 vol. % olivine, which was deformed under similar conditions in D-DIA, although EBSD data were not provided for samples with higher antigorite fractions. Notably, Ohuchi and Irifune (2013) documented B- and C-type olivine CPO formation in dry olivine at pressures exceeding ~7 GPa. However, pressure does not appear to be the controlling factor in this study, as both HP and LP experimental runs produced consistent results (Fig. 5 and 6). Instead, the formation of A- or B- type CPO, and the subsequent transition to C-type CPO is more likely driven by the presence of a weaker antigorite phase in the mixture, rather than by deformation pressure or water concentration in olivine.

As we mentioned, in this study, no dehydration reactions were observed during the experimental runs. However, in natural hydrous mantle wedge environments, both C- and B-type olivine CPO may form through topotactic growth after the dehydration breakdown of antigorite (Boudier et al., 2010; Brownlee et al., 2013; Nagaya et al., 2014; Liu et al., 2021; 2024). Thus, the geological implications of the olivine CPO transition with reduced serpentinization should be evaluated on a case-by-case basis with caution.

On the other hand, Hilairet et al. (2024) and Wallis et al. (2011) proposed that increasing the antigorite fraction weakens the olivine CPO due to reduced stress on olivine. However, our findings show an opposite trend, with lower M- and J- indices in the Atg20/Ol80 sample (Fig. S9b), likely linked to the CPO transition of olivine. Future studies on intermediate compositions are needed to resolve these discrepancies.

As discussed in Section 3.1, the stress and microstructure variations in this study has revealed the framework transition of the two-phase mixtures occurs between 20 and 50 vol. % antigorite. Hilairet et al. (2024), conducting similar D-DIA experiments on antigorite-olivine mixtures with antigorite fractions between 5 and 50 vol. %, proposed that the mechanical behavior of the mixtures changes between 10 and 20 vol. % antigorite. The observed discrepancy in terms of the critical volume fraction of antigorite required for the LBF to LWL transition may be attributed to differences in starting materials: we utilized pre-sintered two-phase aggregates, whereas Hilairet et al. (2024) used hand-pressed mineral powders. Grain size variations may also contribute to these differences. Nonetheless, we suggest that LBF likely represents the mechanical framework for a mantle wedge with a lower degree of serpentinization. Determining the exact threshold for the LBF-IWL transition is challenging. As shown by the gradual movement of the (100) and (010) poles in the X-Z plane associated with decreased antigorite fraction (Fig. 6), the transition is likely gradual rather than abrupt. As a matter of fact, the importance of transitional structure with a moderate amount of strong and weak phase has been highlighted by Ji et al. (2004). Moreover, IWL structure is likely easier to form in two-phase mixtures with large strains, where smaller grains of strong phase are harder to get interconnected with each other. Therefore, the threshold of LBF to IWL transition should vary with the strains of the mantle wedge inside the Earth.

Another key observation in this study is that the observation of A- to C-type olivine CPO transition under the influence of framework of the two-phase mixtures. Specifically, the A- to C-type olivine CPO transition coincides with the formation of LBF structure with decreasing antigorite fraction. The C-type olivine CPO in Atg50/Ol50 with pre-existing CPOs might indicate that the pre-existing CPOs may help promote LBF formation. Although EBSD results for samples Atg70/Ol30 and Atg50/Ol50 both show C-type olivine CPO, the gradual movements of (100) and (010) poles in the PFs derived from EBSD measurements are still observable (Fig. S8), consistent with XRD observations (Fig. 6).

5. Geophysical Implications

5.1 Strength of the antigorite-olivine mixtures and decoupling between slab and mantle wedge

The formation of hydrous minerals (such as serpentine and talc) atop the slab, can reduce friction between the slab and the mantle wedge, as their viscosity is likely lower than that of anhydrous upper mantle minerals like olivine (e.g., Hilairet et al., 2007; Hirauchi and Katayama, 2013; Gasc et al., 2017). This reduction in viscosity is thought to play a key role in slab-mantle decoupling at depths of ~70-80 km, where extensive serpentinization typically occurs (Montési & Hirth, 2003; Kneller et al., 2005; 2007; Wada et al., 2008). However, recent studies have suggested that the viscosity contrast between a thin serpentinite layer and surrounding mantle may not be sufficient to cause significant slab-mantle decoupling (Hirauchi and Katayama, 2013; Hirauchi et al., 2020; Shao et al., 2021). In this study, the estimated stresses of antigorite are lower than those estimated from Hilairet et al. (2024), which is expected since the experiments in this study were conducted at higher temperatures. Similarly, studies involving lower-temperature deformation of antigorite (Hirauchi et al. 2020, and Shao et al. 2021) typically report higher stresses. Additionally, discrepancies in stress estimates may stem from the limited antigorite diffraction peaks that are processable, as we indexed only (001) and (102), while Hilairet et al. (2024) indexed only (001).

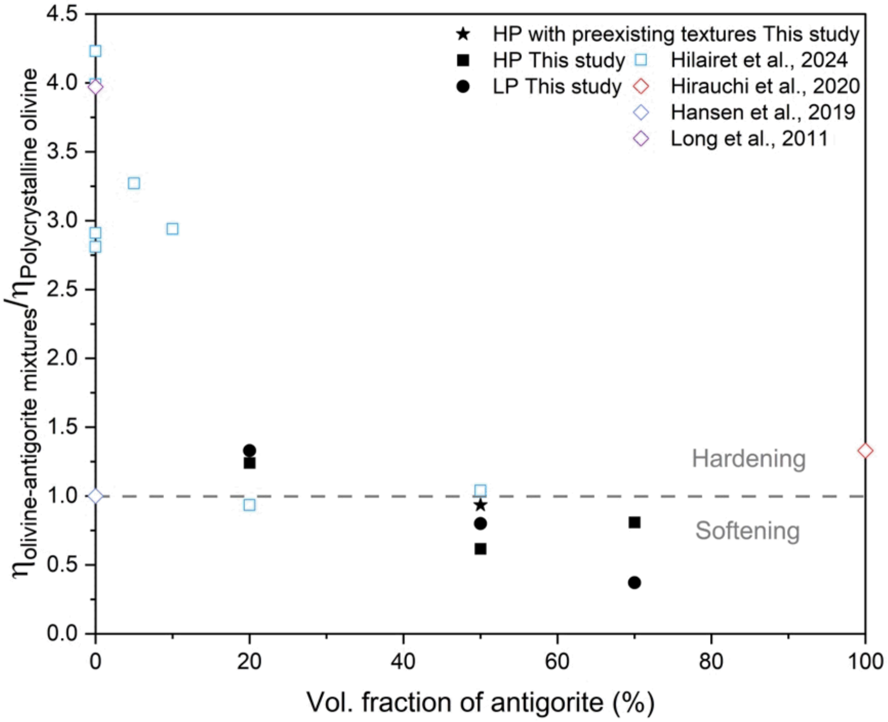

Fig. 10. Viscosity contrast between antigorite-olivine two-phase mixtures determined in this study, Hilairet et al. (2024) and polycrystalline olivine in Hansen et al. (2019) as a function of the antigorite fraction. Additional data on olivine (Long et al., 2011; Hilairet et al., 2024) and antigorite (Chernak and Hirth. 2010; Hirauchi et al., 2020) aggregates are included for comparison.

To further evaluate the strength of serpentinized peridotite relative to anhydrous peridotite, we calculated the viscosity contrast between the antigorite-olivine two-phase mixtures (This study, Hilairet et al., 2024) and single-phase olivine (Hansen et al., 2019), which is the same as the way applied in Hilairet et al. (2024). The viscosity of olivine varies widely, from values similar to polycrystalline antigorite at the lower end to approximately 4 times higher at the upper end. The reference viscosity value in this study is based on the lower bound of olivine viscosity from Hansen et al. (2019). As shown in Fig. 10, when the antigorite fraction exceeds 50%, the viscosity of the two-phase mixture is lower than that of either olivine or antigorite, consistent with findings from Hirauchi and Katayama (2013), Hirauchi et al. (2020), and Shao et al. (2021). This suggests the formation of the IWL structure reduces the mixture's strength.

In contrast, when the antigorite fraction is ≤ 20%, the viscosity of the two-phase mixtures exceeds that of olivine determined by Hansen et al. (2019). The higher viscosity contrast observed at ≤ 10 vol. % antigorite might result from the local hardening of olivine under low strain rate deformation (Handy, 1990; Hilairet et al., 2024). In this scenario, most antigorite grains might be oriented perpendicular to the maximum stress direction and unable to accommodate further deformation, creating a "locked geometry" proposed by Amiguet et al. (2012). In this case, olivine shares the isostress state with antigorite. Notably, the viscosity values of Atg20/Ol80 determined in this study are still lower than the upper bound values for olivine viscosity in Long et al. (2011) and Hilairet et al. (2024). In fact, the viscosity of antigorite aggregate estimated by Chernak and Hirth (2010) and Hirauchi et al. (2020) is higher than that of olivine by Hansen et al. (2019). Chernak and Hirth (2010) suggested that the viscosity contrast between olivine and antigorite is only approximately 1 – 2, which indicates that the reported viscosity ranges for pure olivine and antigorite aggregates may reflect differences in experimental conditions or setups across studies. Combining the viscosity data of antigorite-olivine two-phase mixture from this study and Hilairet et al. (2024), we found that a low degree of serpentinization (< 20%) is unlikely to reduce the friction between the slab and mantle wedge, potentially even enhancing coupling and hindering slab subduction, depending on the petrologic composition of the overlaying mantle. However, when serpentinization exceeds ≥ 70%, the viscosity of the antigorite-olivine two-phase mixture decreases. If the peridotite in the ambient mantle has a viscosity similar to the upper bound value for olivine (Long et al. 2011), a highly serpentinized mantle with ≥70% antigorite has a better chance to serve as a decoupling zone, as a viscosity contrast of ~10 is typically required for effective decoupling (Hirauchi and Katayama. 2013). Alternatively, if the ambient mantle has a viscosity closer to the lower bound of olivine (Hansen et al. 2019), even 70% serpentinization may not induce decoupling. Pre-existing CPOs, which favor the formation of LBF, appear to increase the strength of the mixtures (Fig. 10). Consequently, slabs with fossil fabrics inherited from past geological processes can be stronger than those without such histories.

5.2 Shear-wave splitting observations with different degrees of serpentinization

Both trench-parallel and trench-perpendicular shear-wave splitting have been observed (Long and Becker. 2010; Becker and Lebedev. 2021), with trench-parallel shear-wave splitting being more widespread. These observations are likely caused by the mantle flow-induced CPO of anisotropic minerals along the seismic ray path. Because shear-wave splitting measurements have poor vertical resolution, anisotropy can originate anywhere along the path, including the complicated mantle wedge (Long and Wirth, 2013; Becker and Lebedev, 2021). While the mantle wedge is dominated by 2D corner flow induced by slab subduction, 3D trench-parallel flow can also develop beneath and above the slab (Long and Silver, 2008). Although the combination of A-type olivine CPO with 3D trench-parallel flow is a potential explanation for trench-parallel anisotropy, we focus here on another mechanism: the combined 2D corner flow with deformed serpentinized mantle peridotite.

The antigorite-olivine mixtures deformed in this study serve as a simplified analog for serpentinized mantle peridotite. The deformation geometry in this study (axial shortening) differs from that in the mantle wedge (close to simple shear), making direct quantitative comparisons with seismic observations challenging. The maximum AVs determined for all run products in this study are expected to be significantly lower than natural systems with much higher shear strain deformed under simple shear (Fig. 7; Fig. S10). However, the relative textural strength and anisotropy among the 7 run products, as outlined in section 3.3, can still be compared to provide insights into the effect of serpentinization degree on seismic anisotropy in the mantle wedge.

The seismic anisotropy of the final two-phase antigorite-olivine mixture includes contributions from both antigorite and olivine. Liu et al. (2020) developed a mantle wedge anisotropy model, which is antigorite fraction-dependent based on EBSD measurements of natural samples with varying proportions of antigorite- and olivine-rich layers, linking these findings to subduction zones with different subduction angles. However, in this study, we've found the AVs and AVp of samples Atg50/Ol50 and Atg70/Ol30 are very similar, both of which are markedly higher than that of sample Atg20/Ol80 (Fig. 9c). This trend is consistent with the reported anisotropy of naturally deformed serpentinite samples in Jung. (2011), who reported max AVs values of 23.2% and 22.81% for samples with 40 vol. % and 78 vol. % antigorite, respectively, compared to 36.53% and 34.01% for samples containing 87 vol. % and 93 vol. % antigorite. Thus, the anisotropy of antigorite-olivine mixtures may not increase linearly with the degree of serpentinization, but establishing a more detailed trend requires data for a broader range of antigorite volume fractions. Contributions of other highly anisotropic phases, such as clinopyroxenes (e.g., Hao et al. 2019, 2021), also need to be considered to better represent the lithology of a realistic slab.

It is also worth noting that the AVs value of antigorite-olivine mixtures decreases as a result of pre-existing CPOs, as mentioned in section 3.3. This decrease is directly linked to the observed weak CPOs of both antigorite and olivine. Therefore, we suggest that slabs with fossil fabrics are likely to show lower seismic anisotropy. However, the persistence of pre-existing CPOs in actively subducting slabs remains uncertain, making their significance over geological time scales questionable.

6. Conclusion

In this study, we studied the variation of stress, strength, CPO, and anisotropy of the olivine and antigorite mixtures relative to the antigorite volume fractions through D-DIA experiments conducted at two different pressure ranges: 6.44 GPa-7.09 GPa and 2.56 GPa-3.78 GPa. Our key findings are:

(1) The transition of olivine CPO from A- to C-type occurs when the antigorite fraction decreases to 20%, coinciding with the formation of LBF structures in the two-phase mixture. The presence of pre-existing CPOs can promote LBF formation in mixtures with 50 vol. % antigorite.

(2) Slab-mantle decoupling is unlikely when antigorite fraction is limited to 20 % or less, since the strength of the mixtures may even increase. However, decoupling is more likely to take place if the degree of serpentinization exceeds 70%, provided that the ambient mantle is strong enough to generate a sufficiently high viscosity contrast (>10). Pre-existing CPOs seem to enhance the strength of the mixtures.

(3) Shear wave velocity anisotropy in serpentinized peridotite generally increases with antigorite volume fractions, although the relationship is likely nonlinear. The presence of pre-

existing CPOs could reduce the anisotropy value by altering microstructures and CPOs, although their geological significance depends on how long these fossil CPOs persist during subduction.

Acknowledgement

This project is funded by NSF-EAR 2243184 (JSZ). LM acknowledges support from the US Department of Energy, National Nuclear Security Administration, through the Chicago/DOE Alliance Center (DE-NA0004153). LLNL-JRNL-2003596. This work was performed under the auspices of the U.S. Department of Energy by Lawrence Livermore National Laboratory under Contract DE-AC52-07NA2.We sincerely thank George Harlow from AMNH for generously providing the antigorite samples for this study, Mike Spilde and Carl Agee for their help with sample preparation. Portions of this work were performed at GeoSoilEnviroCARS (The University of Chicago, Sector 13), Advanced Photon Source, Argonne National Laboratory. GeoSoilEnviroCARS is supported by the National Science Foundation – Earth Sciences via SEES: Synchrotron Earth and Environmental Science (EAR –2223273). This research used resources of the Advanced Photon Source, a U.S. Department of Energy (DOE) Office of Science User Facility operated for the DOE Office of Science by Argonne National Laboratory under Contract No. DE-AC02-06CH11357.

References

Amiguet, E., Reynard, B., Caracas, R., Moortèle, B.V. de, Hilairet, N., Wang, Y., 2012. Creep of phyllosilicates at the onset of plate tectonics. Earth Planet. Sci. Lett. 345, 142–150. https://doi.org/10.1016/j.epsl.2012.06.033

Auzende, A. L., Escartin, J., Walte, N. P., Guillot, S., Hirth, G., Frost, D. J., 2015. Deformation mechanisms of antigorite serpentinite at subduction zone conditions determined from experimentally and naturally deformed rocks. Earth and Planetary Science Letters 411, 229-240. https://doi.org/10.1016/j.epsl.2014.11.053

Bachmann, F., Hielscher, R., Schaeben, H., 2010. Texture Analysis with MTEX – Free and Open Source Software Toolbox. Solid State Phenomena 160, 63–68. https://doi.org/10.4028/www.scientific.net/ssp.160.63

Becker, T.W., Lebedev, S., 2021. Mantle Convection and Surface Expressions. Geophys. Monogr. Ser. 257–282. https://doi.org/10.1002/9781119528609.ch10

Ben Ismail, W., Mainprice, D., 1998. An olivine fabric database; an overview of upper mantle fabrics and seismic anisotropy. Tectonophysics 296, 145–157.

Bezacier, L., Reynard, B., Bass, J.D., Sanchez-Valle, C., Moortèle, B.V. de, 2010. Elasticity of antigorite, seismic detection of serpentinites, and anisotropy in subduction zones. Earth Planet. Sci. Lett. 289, 198–208. https://doi.org/10.1016/j.epsl.2009.11.009

Bezacier, L., Reynard, B., Cardon, H., Montagnac, G., Bass, J.D., 2013. High-pressure elasticity of serpentine and seismic properties of the hydrated mantle wedge. J. Geophys. Res.: Solid Earth 118, 527–535. https://doi.org/10.1002/jgrb.50076

Boudier, F., Baronnet, A., Mainprice, D., 2010. Serpentine Mineral Replacements of Natural Olivine and their Seismic Implications: Oceanic Lizardite versus Subduction-Related Antigorite. J. Pet. 51, 495–512. https://doi.org/10.1093/petrology/egp049

Brantut, N., Schubnel, A., Gueguen, Y., 2011. Damage and rupture dynamics at the brittle-ductile transition: the case of gypsum. J. Geophys. Res., Solid Earth 116.

Brownlee, S.J., Hacker, B.R., Harlow, G.E., Seward, G., 2013. Seismic signatures of a hydrated mantle wedge from antigorite crystal-preferred orientation (CPO). Earth Planet. Sci. Lett. 375, 395–407. https://doi.org/10.1016/j.epsl.2013.06.003

Burdette, E., Hirth, G., 2022. Creep Rheology of Antigorite: Experiments at Subduction Zone Conditions. J. Geophys. Res.: Solid Earth 127. https://doi.org/10.1029/2022jb024260

Burnley, P., 2015. Elastic plastic self-consistent (EPSC) modeling of plastic deformation in fayalite olivine. American Mineralogist Special Collection: Olivine 100, 1424-1433. http://dx.doi.org/10.2138/am-2015-5234CCBYNCND

Burnley, P., Kaboli, S., 2019. Elastic plastic self-consistent (EPSC) modeling of San Carlos olivine deformed in a D-DIA apparatus. American Mineralogist 104, 276-281. https://doi.ord/10.2138/am-2019-6666

Bystricky, M., Kunze, K., Burlini, L., Burg, J.-P., 2000. High Shear Strain of Olivine Aggregates: Rheological and Seismic Consequences. Science 290, 1564–1567. https://doi.org/10.1126/science.290.5496.1564

Chernak, L.J., Hirth, G., 2010. Deformation of antigorite serpentinite at high temperature and pressure. Earth Planet. Sci. Lett. 296, 23–33. https://doi.org/10.1016/j.epsl.2010.04.035

Escartin, J., Andreani, M., Hirth, G., Evans, B., 2008. Relationships between the microstructural evolution and the rheology of talc at elevated pressures and temperatures. Earth Planet. Sci. Lett. 268, 463–475.

Evans, B. W., Hattori, K., Baronnet, A., 2013. Serpentinite: What, why, where? Elements 9(2), 99–106. https://doi.org/10.2113/ gselements.9.2.99

Ferrand, T. P., 2017. Reproduction expérimentale d'analogues de séismes mantelliques par déshydratation de l'antigorite & Comparaison à des pseudotachylites naturelles (doctoral dissertation) PSL Research University.

Ferrand, T.P., Hilairet, N., Incel, S., Deldicque, D., Labrousse, L., Gasc, J., Renner, J., Wang, Y., II, H.W.G., Schubnel, A., 2017. Dehydration-driven stress transfer triggers intermediate-depth earthquakes. Nat. Commun. 8, 15247. https://doi.org/10.1038/ncomms15247

Gasc, J., Hilairet, N., Yu, T., Ferrand, T., Schubnel, A., Wang, Y., 2017. Faulting of natural serpentinite: Implications for intermediate-depth seismicity. Earth Planet. Sci. Lett. 474, 138–147. https://doi.org/10.1016/j.epsl.2017.06.016

Guo, Z., Lin, J., Zhang, J., Zhang, F., Yang, X., Cheng, Z., Zhou, P., 2024. The effect of pre-existing fabrics on plate bending and seismicity in Alaska subduction zone. Terra Nova 36, 210–216. https://doi.org/10.1111/ter.12699

Handy, M.R., 1994. Flow laws for rocks containing two non-linear viscous phases: A phenomenological approach. Journal of Structural Geology 16, 287-301.

Handy, M.R., 1990. The solid-state flow of polymineralic rocks. Journal of Geophysical Research: Solid Earth 95, 8647-8661.

Hansen, L.N., Kumamoto, K.M., Thom, C.A., Wallis, D., Durham, W.B., Goldsby, D.L., Breithaupt, T., Meyers, C.D., Kohlstedt, D.L., 2019. Low-Temperature Plasticity in Olivine: Grain Size, Strain Hardening, and the Strength of the Lithosphere. J. Geophys. Res.: Solid Earth 124, 5427–5449. https://doi.org/10.1029/2018jb016736

Hansen, L.N., David, E.C., Brantut, N., Wallis, D., 2020. Insight into the microphysics of antigorite deformation from spherical nanoindentation. Philos. Trans. R. Soc. A 378, 20190197. https://doi.org/10.1098/rsta.2019.0197

Hao, M., Zhang, J.S., Pierotti, C.E., Ren, Z., Zhang, D. 2019. High‐pressure single‐crystal elasticity and thermal equation of state of omphacite and their implications for the seismic properties of eclogite in the Earth's interior. Journal of Geophysical Research: Solid Earth, 124, 2368–2377. https://doi.org/10.1029/2018JB016964

Hao, M., Zhang, J.S., Zhou, W.-Y., Wang, Q., 2021. Seismic visibility of eclogite in the Earth's upper mantle—Implications from high pressure-temperature single-crystal elastic properties of omphacite. Journal of Geophysical Research: Solid Earth,126, e2021JB021683. https://doi.org/10.1029/2021JB021683

Hilairet, N., Reynard, B., Wang, Y., Daniel, I., Merkel, S., Nishiyama, N., Petitgirard, S., 2007. High-Pressure Creep of Serpentine, Interseismic Deformation, and Initiation of Subduction. Science 318(5858), 1910–1913. https://doi.org/10.1126/science.1148494

Hilairet, N., Wang, Y., Sanehira, T., Merkel, S., Mei, S., 2012. Deformation of olivine under mantle conditions: An in situ high-pressure, high-temperature study using monochromatic synchrotron radiation. Journal of Geophysical Research 117, B01203. https://doi.org/10.1029/2011JB008498

Hilairet, N., Guignard, J., Ferrand, T. P.,Merkel, S., Raterron, P., Ildefonse, B.,et al., 2024. Stress balance in syntheticserpentinized peridotites deformed atsubduction zone pressures. Journal of Geophysical Research: Solid Earth 129, e2023JB028073. https://doi.org/10.1029/2023JB028073

Hirauchi, K. I., Michibayashi, K., Ueda, H., Katayama, I., 2010. Spatial variations in antigorite fabric across a serpentinite subduction channel: Insights from the Ohmachi Seamount, Izu-Bonin frontal arc. Earth and Planetary Science Letters 299(1-2), 196-206.

Hirauchi, K., Katayama, I., 2013. Rheological contrast between serpentine species and implications for slab–mantle wedge decoupling. Tectonophysics 608, 545–551. https://doi.org/10.1016/j.tecto.2013.08.027

Hirauchi, K., Katayama, I., Kouketsu, Y., 2020. Semi-brittle deformation of antigorite serpentinite under forearc mantle wedge conditions. J. Struct. Geol. 140, 104151. https://doi.org/10.1016/j.jsg.2020.104151

Hirauchi, K., Nagata, Y., Kataoka, K., Oyanagi, R., Okamoto, A., Michibayashi, K., 2021. Cataclastic and crystal-plastic deformation in shallow mantle-wedge serpentinite controlled by cyclic changes in pore fluid pressures. Earth Planet. Sci. Lett. 576, 117232. https://doi.org/10.1016/j.epsl.2021.117232

Horn, C., Bouilhol, P., Skemer, P., 2020. Serpentinization, Deformation, and Seismic Anisotropy in the Subduction Mantle Wedge. Geochem., Geophys., Geosystems 21, e2020GC008950. https://doi.org/10.1029/2020gc008950

Grove, T.L., Till, C.B., Krawczynski, M.J., 2012. The Role of H2O in Subduction Zone Magmatism. Annu. Rev. Earth Planet. Sci. 40, 413–439. https://doi.org/10.1146/annurev-earth-042711-105310

Guillot, S., Schwartz, S., Reynard, B., Agard, P., Prigent, C., 2015. Tectonic significance of serpentinites. Tectonophysics 646, 1–19. https://doi.org/10.1016/j.tecto.2015.01.020

Ji, S., Wang, Q., Xia, B., Marcotte, D., 2004. Mechanical properties of multiphase materials and rocks: a phenomenological approach using generalized means. J. Struct. Geol. 26, 1377–1390. https://doi.org/10.1016/j.jsg.2003.12.004

Ji, S., Li, A., Wang, Q., Long, C., Wang, H., Marcotte, D., Salisbury, M., 2013. Seismic velocities, anisotropy, and shear-wave splitting of antigorite serpentinites and tectonic implications for subduction zones. J. Geophys. Res.: Solid Earth 118, 1015–1037. https://doi.org/10.1002/jgrb.50110

Jung, H., Karato, S., 2001. Water-Induced Fabric Transitions in Olivine. Science 293, 1460–1463. https://doi.org/10.1126/science.1062235

Jung, H., Katayama, I., Jiang, Z., Hiraga, T., Karato, S., 2006. Effect of water and stress on the lattice-preferred orientation of olivine. Tectonophysics 421, 1–22. https://doi.org/10.1016/j.tecto.2006.02.011

Jung, H., Mo, W., Green, H.W., 2009a. Upper mantle seismic anisotropy resulting from pressure-induced slip transition in olivine. Nat. Geosci. 2, 73–77. https://doi.org/10.1038/ngeo389

Jung, H., Fei, Y., Silver, P.G., Green, H.W., 2009b. Frictional sliding in serpentine at very high pressure. Earth Planet. Sci. Lett. 277, 273–279. https://doi.org/10.1016/j.epsl.2008.10.019

Jung, H., 2011. Seismic anisotropy produced by serpentine in mantle wedge. Earth Planet. Sci. Lett. 307, 535–543. https://doi.org/10.1016/j.epsl.2011.05.041

Jung, H., 2018. Erratum to: Crystal preferred orientations of olivine, orthopyroxene, serpentine, chlorite, and amphibole, and implications for seismic anisotropy in subduction zones: a review. Geosci. J. 22, 523–550. https://doi.org/10.1007/s12303-018-0009-0

Katayama, I., Jung, H., Karato, S.-I., 2004. New type of olivine fabric from deformation experiments at modest water content and low stress. Geology 32 (12): 1045–1048. https://doi.org/10.1130/G20805.1

Kumamoto, K.M., Hansen, L.N., Breithaupt, T., Wallis, D., Li, B., Armstrong, D.E.J., Goldsby, D.L., Li, Y. (Will), Warren, J.M., Wilkinson, A.J., 2024. The Effect of Intracrystalline Water on the Mechanical Properties of Olivine at Room Temperature. Geophys. Res. Lett. 51. https://doi.org/10.1029/2023gl106325

Katayama, I., Karato, S., 2006. Effect of temperature on the B- to C-type olivine fabric transition and implication for flow pattern in subduction zones. Phys. Earth Planet. Inter. 157, 33–45. https://doi.org/10.1016/j.pepi.2006.03.005

Katayama, I., Hirauchi, K.-I., Michibayashi, K., Ando, J.-I., 2009. Trench-parallel anisotropy produced by serpentine deformation in the hydrated mantle wedge. Nature 461, 1114–1118.

Kayima, S.I and Kobayashi, Y., 2000. Seismological evidence for the existence of serpentinized wedge mantle. Geophysical Research Letters 27 (6), 819-822. https://doi.org/10.1029/1999GL011080

Kenyon, L., Wada, I., 2022. Mantle Wedge Seismic Anisotropy and Shear Wave Splitting: Effects of Oblique Subduction. Journal of Geophysical Research: Solid Earth 127, e2021JB022752. https://doi.org/10.1029/2021JB022752

Kneller, E.A., Keken, P.E. van, Karato, S., Park, J., 2005. B-type olivine fabric in the mantle wedge: Insights from high-resolution non-Newtonian subduction zone models. Earth Planet. Sci. Lett. 237, 781–797. https://doi.org/10.1016/j.epsl.2005.06.049

Kneller, E.A., Keken, P.E. van, Katayama, I., Karato, S., 2007. Stress, strain, and B-type olivine fabric in the fore-arc mantle: Sensitivity tests using high-resolution steady-state subduction zone models. J. Geophys. Res.: Solid Earth 112. https://doi.org/10.1029/2006jb004544

Kneller, E.A., Long, M.D., Keken, P.E. van, 2008. Olivine fabric transitions and shear wave anisotropy in the Ryukyu subduction system. Earth Planet. Sci. Lett. 268, 268–282. https://doi.org/10.1016/j.epsl.2008.01.004

Lin, F., Giannetta, M., Jugle, M., Couper, S., Dunleavy, B., Miyagi, L., 2019. Texture Development and Stress–Strain Partitioning in Periclase + Halite Aggregates. Minerals 9, 679. https://doi.org/10.3390/min9110679

Liu, G., Zhou, Y., He, C., Yao, W., Liu, J., Zhang, Y., 2016. An experimental study of effect of pre-existing fabric on deformation of foliated mylonite at high temperature and pressure. Geol. J. 51, 92–112. https://doi.org/10.1002/gj.2611

Liu, W., Zhang, J., Cao, Y., Jin, Z., 2020. Geneses of Two Contrasting Antigorite Crystal Preferred Orientations and Their Implications for Seismic Anisotropy in the Forearc Mantle. J. Geophys. Res.: Solid Earth 125. https://doi.org/10.1029/2020jb019354

Liu, W.L., Qi, H.W., Zhang, J.F., Wu, X., Li, J.F., Zhao, R., Wang, Y.F., Jin, Z.M., 2021. Hydrostatic Dehydration Fabrics of Antigorite at High Pressure and High Temperature: Implications for Trench Parallel Seismic Anisotropy at Convergent Plate Boundaries. J. Geophys. Res.: Solid Earth 126. https://doi.org/10.1029/2021jb021671

Liu, W., Cao, Y., Li, J., Song, M., Xu, H., Wang, Y., Wu, X., Zhang, J., Kohlstedt, D.L., 2024. Type-B Crystallographic Preferred Orientation in Olivine Induced by Dynamic Dehydration of Antigorite in Forearc Regions. J. Geophys. Res.: Solid Earth 129. https://doi.org/10.1029/2023jb027929

Long, H., Weidner, D.J., Li, L., Chen, J., Wang, L., 2011. Deformation of olivine at subduction zone conditions determined from in situ measurements with synchrotron radiation. Phys. Earth Planet. Inter. 186, 23–35. https://doi.org/10.1016/j.pepi.2011.02.006

Long, M. D., and van der Hilst, R. D., 2006. Shear wave splitting from local events beneath the Ryukyu arc: Trench-parallel anisotropy in the mantle wedge. Physics of the Earth and Planetary Interiors 155(3–4), 300–312. https://doi.org/10.1016/j.pepi.2006.01.003

Long, M.D., Silver, P.G., 2008. The Subduction Zone Flow Field from Seismic Anisotropy: A Global View. Science 319, 315–318. https://doi.org/10.1126/science.1150809

Long, M.D., Becker, T.W., 2010. Mantle dynamics and seismic anisotropy. Earth Planet. Sci. Lett. 297, 341–354. https://doi.org/10.1016/j.epsl.2010.06.036

Long, M. D., and Wirth, E. A., 2013. Mantle flow in subduction systems: The mantle wedge flow field and implications for wedge processes. Journal of Geophysical Research: Solid Earth 118(2), 583–606. https://doi.org/10.1002/jgrb.50063

Lutterotti, L., Matthies, S., Wenk, H. R., Schultz, A. S., & Richardson, J. W., 1997. Combined texture and structure analysis of deformed limestone from time-of-flight neutron diffraction spectra. Journal of Applied Physics 81(2), 594–600. https://doi.org/10.1063/1.364220

Mackwell, S.J., Kohlstedt, D.L., Paterson, M.S., 1985. The role of water in the deformation of olivine single crystals. J. Geophys. Res.: Solid Earth 90, 11319–11333. https://doi.org/10.1029/jb090ib13p11319

Matthies, S., Vinel, G. W., 1982. On the reproduction of the orientation distribution function of texturized samples from reduced pole figures using the conception of a conditional ghost correction. Physica status solidi (b) 112(2), K111-K114.

Montési, L.G.J., Hirth, G., 2003. Grain size evolution and the rheology of ductile shear zones: from laboratory experiments to postseismic creep. Earth Planet. Sci. Lett. 211, 97–110. https://doi.org/10.1016/s0012-821x(03)00196-1

Morales, L., Mainprice, D., Kern, H., 2018. Olivine-antigorite orientation relationships: Microstructures, phase boundary misorientations and the effect of cracks in the seismic properties of serpentinites, Tectonophysics, 724–725, 93–115. https://doi.org/10.1016/j.tecto.2017.12.009

Nagaya, T., Wallis, S.R., Kobayashi, H., Michibayashi, K., Mizukami, T., Seto, Y., Miyake, A., Matsumoto, M., 2014. Dehydration breakdown of antigorite and the formation of B-type olivine CPO. Earth Planet. Sci. Lett. 387, 67–76. https://doi.org/10.1016/j.epsl.2013.11.025

Nishii, A., Wallis, S.R., Mizukami, T., Michibayashi, K., 2011. Subduction related antigorite CPO patterns from forearc mantle in the Sanbagawa belt, southwest Japan. Journal of Structural Geology 33, 1436-1445. https://doi.org/10.1016/j.jsg.2011.08.006

Ohuchi, T., Kawazoe, T., Nishihara, Y., Irifune, T., 2012. Change of olivine a-axis alignment induced by water: Origin of seismic anisotropy in subduction zones. Earth Planet. Sci. Lett. 317, 111–119. https://doi.org/10.1016/j.epsl.2011.11.022

Ohuchi, T., Irifune, T., 2013. Development of A-type olivine fabric in water-rich deep upper mantle. Earth Planet. Sci. Lett. 362, 20–30. https://doi.org/10.1016/j.epsl.2012.11.029

Padrón-Navarta, J.A., Tommasi, A., Garrido, C.J., Sánchez-Vizcaíno, V.L., 2012. Plastic deformation and development of antigorite crystal preferred orientation in high-pressure serpentinites. Earth Planet. Sci. Lett. 349, 75–86. https://doi.org/10.1016/j.epsl.2012.06.049

Proctor, B., Hirth, G., 2016. “Ductile to brittle” transition in thermally stable antigorite gouge at mantle pressures. J. Geophys. Res.: Solid Earth 121, 1652–1663. https://doi.org/10.1002/2015jb012710

Satta, N., Morales, L.F.G., Criniti, G., Kurnosov, A., Ballaran, T.B., Speziale, S., Marquardt, K., Capitani, G.C., Marquardt, H., 2022. Single-Crystal Elasticity of Antigorite at High

Pressures and Seismic Detection of Serpentinized Slabs. Geophys. Res. Lett. 49. https://doi.org/10.1029/2022gl099411

Shao, T., Ji, S., Kondo, Y., Michibayashi, K., Wang, Q., Xu, Z., Sun, S., Marcotte, D., Salisbury, M.H., 2014. Antigorite-induced seismic anisotropy and implications for deformation in subduction zones and the Tibetan Plateau. J. Geophys. Res.: Solid Earth 119, 2068–2099. https://doi.org/10.1002/2013jb010661

Shao, T., Zhou, Y., Song, M., Ma, X., Zhang, L., Yao, W., Dang, J., Li, J., 2021. Deformation of Antigorite and Its Geological Implications. J. Geophys. Res.: Solid Earth 126. https://doi.org/10.1029/2021jb021650

Singh, A. K., C. Balasingh, H. K. Mao, R. J. Hemley, and J. F. Shu (1998), Analysis of lattice strains measured under nonhydrostatic pressure, J. Appl. Phys., 83(12), 7567–7575, doi:10.1063/1.367872

Soda, Y., Takagi, H., 2010. Sequential deformation from serpentinite mylonite to metasomatic rocks along the Sashu Fault, SW Japan. J. Struct. Geol. 32, 792–802. https://doi.org/10.1016/j.jsg.2010.05.003

Soda, Y., Wenk, H. R., 2014. Antigorite crystallographic preferred orientations in serpentinites from Japan. Tectonophysics, 615–616, 199–212. https://doi.org/10.1016/j.tecto.2013.12.016

van Keken, P. E., 2003. The structure and dynamics of the mantle wedge. Earth and Planetary Science Letters 215(3–4), 323–338. https://doi.org/10.1016/S0012-821X(03)00460-6

Skemer, P., Katayama, I., Jiang, Z., Karato, S., 2005. The misorientation index: development of a new method for calculating the strength of lattice-preferred orientation. Tectonophysics 411, 157–167.

Tange, Y., Nishihara, Y. and Tsuchiya, T., 2009. Unified analyses for P‐V‐T equation of state of MgO: A solution for pressure‐scale problems in high P‐T experiments. Journal of Geophysical Research: Solid Earth, 114(B3)

Wada, I., Wang, K., He, J., Hyndman, R. D., 2008. Weakening of the subduction interface and its effects on surface heat flow, slab dehydration, and mantle wedge serpentinization. Journal of Geophysical Research: Solid Earth 113(4), 1–15. https://doi.org/10.1029/2007JB005190

Wallis, S.R., Kobayashi, H., Nishii, A., Mizukami, T., Seto, Y., 2011. Obliteration of olivine crystallographic preferred orientation patterns in subduction-related antigorite-bearing mantle peridotite: an example from the HigashiAkaishi body, SW Japan. Geol. Soc., Lond., Spéc. Publ. 360, 113–127. https://doi.org/10.1144/sp360.7

Wang, H., Wu, P.D., Tomé, C.N., Huang, Y., 2010. A finite strain elastic–viscoplastic self-consistent model for polycrystalline materials. Journal of the Mechanics and Physics of Solids 58(4), b594-612, https://doi.org/10.1016/j.jmps.2010.01.004

Wenk, H. R., Matthies, S., Donovan, J., & Chateigner, D. (1998). BEARTEX: a Windows-based program system for quantitative texture analysis. Journal of Applied Crystallography, 31(2), 262-269.

Wenk, H.-R., Lutterotti, L., Kaercher, P., Kanitpanyacharoen, W., Miyagi, L., Vasin, R., 2014. Rietveld texture analysis from synchrotron diffraction images. II. Complex multiphase materials and diamond anvil cell experiments. Powder Diffr. 29, 220–232.

Wiens, D., Conder, J., Faul, U., 2008. The Seismic Structure and Dynamics of the Mantle Wedge. Annual Review of Earth and Planetary Sciences 36, 421-455. https://doi.org/10.1146/annurev.earth.22.092203.122633

Wu, M.Q., Wang, Q., Wang, H.B., 2025. Thermal structure, fluid activity and earthquake mechanisms of oceanic subduction zones. Science China: Earth Sciences. (In press)

Yu, T., Wang, Y., Rivers, M.L., Sutton, S.R., 2019. An upgraded and integrated large-volume high-pressure facility at the GeoSoilEnviroCARS bending magnet beamline of the Advanced Photon Source. C. R. Geosci. 351, 269–279. https://doi.org/10.1016/j.crte.2018.09.006

Zhang, J.S., Bass, J.D., 2016. Sound velocities of olivine at high pressures and temperatures and the composition of Earth's upper mantle. Geophys. Res. Lett. 43, 9611–9618. https://doi.org/10.1002/2016gl069949

Zhang, S., Karato, Si., 1995. Lattice preferred orientation of olivine aggregates deformedin simple shear. Nature 375, 774–777. https://doi.org/10.1038/375774a0

Zhang, W., Xia, X., Eiichi, T., Li, L., Yang, Q., Zhang, Y., Yang, Y., Liu, M., Lai, C., 2019. Optimization of SIMS analytical parameters for water content measurement of olivine. Surf. Interface Anal. 52, 224–233. https://doi.org/10.1002/sia.6729

Supplementary materials for

In-situ deformation of antigorite-olivine two-phase mixtures: implications for the dynamics and seismic anisotropy in the mantle wedge

Rose Hurlow[a, b#], Wenhao Su[c#], Wen-Yi Zhou[c], Feng Lin[d], Lowell Miyagi[d], Timothy Officer[e], Tony Yu[e], Yanbin Wang[e], Meiqian Wu[f], Qin Wang[f], Jin Zhang[a,c*]

g. Department of Earth and Planetary Sciences, University of New Mexico, Albuquerque, NM, 87131, USA
h. Lawrence Livermore National Lab, 7000 East Avenue, Livermore, CA, 94550, USA
i. Department Geology and Geophysics, Texas A&M University, College Station, TX, 77843, USA
j. Department of Geology and Geophysics, The University of Utah, Salt Lake City, UT, 84112, USA
k. Center for Advanced Radiation Sources, University of Chicago, Chicago, IL, 60439, USA
l. School of Earth Science and Engineering, Nanjing University, Nanjing, Jiangsu, 210023, China

# made equal contribution to this study; *corresponding author.

This file includes:

Supplementary Text S1 to S3
Equations S1 to S5
Table S1 to S2
Figures S1 to S10
Supplementary References

Supplementary Text S1: EBSD experiments and results

We polished thin sections of two recovered samples (Atg30/Ol70 and Atg50/Ol50) using 0.3 micron polishing cloth and Al_2O_3 polishing liquid, followed by vibration polishing to remove the mechanical damage. The crystallographic preferred orientations (CPOs) of olivine and antigorite were measured on a scanning electron microscope JEOL JSM-6490 equipped with an Oxford Nordlys-S EBSD detector and the Aztec software at State Key Laboratory for Mineral Deposits Research, Nanjing University, China. The thin section was tilted 70° compared to the normal configuration and measured with a working distance of 18 – 24 mm, an accelerating voltage of 20 kV and a beam current of 4 nA. The EBSD patterns were indexed using the crystal structure of forsterite (Smyth and Hazen, 1973) and antigorite (Capitani and Mellini, 2004). Automatic identification of antigorite by EBSD mapping was not successful, thus we manually scanned the entire section and indexed the mineral phases according to the pattern quality and the agreement between detected and simulated Kikuchi bands. The indexed results with mean angular deviation (MAD) values of <1 are considered desirable for accurate solutions. Crystallographic orientations of olivine and antigorite are plotted as one point per grain in the lower hemisphere equal-area projection according to the reference system of deformation experiments (X = flow direction; Z = direction of compression) using the open-source software MTEX (Bachmann et al., 2010).

As shown in Fig. S8, olivine grains in samples Atg70/Ol30 and Atg50/Ol50 show dominant (010) poles parallel to the compressional direction Z, consistent with the ODF obtained from XRD experiments. Additionally, olivine of sample Atg50/Ol50 also exhibits relatively higher maxima of (100) poles align with compressional direction Z, suggesting a formation of C-type CPO during the formation of load-bearing framework structures in the antigorite-olivine mixtures. This is consistent with the pole figure analyzed from the X-ray diffraction (XRD) data (Fig. 6). For antigorite, unfortunately, we only indexed 44 and 13 grains for samples Atg70/Ol30 and Atg50/Ol50, respectively. It is well-known that EBSD experiments on experimentally deformed antigorite samples are exceedingly challenging. However, the plotted pole figure pattern aligns with XRD data (Fig. 6). Notley, the CPO strength and the calculated anisotropy values of recovered samples exceed those processed from XRD data (Table S1, Fig. S10), likely due to the differences between 2D EBSD analysis and 3D bulk sample XRD analysis.

Supplementary Text S2: Lattice Strains and Stress calculations

The D-DIA apparatus applies an axial compression to the sample, resulting in a stress state at the sample center that can be decomposed into hydrostatic and deviatoric components:

$$\sigma_{ij} = \begin{bmatrix} \sigma_{11} & 0 & 0 \\ 0 & \sigma_{22} & 0 \\ 0 & 0 & \sigma_{33} \end{bmatrix}$$

$$= \begin{bmatrix} \sigma_P & 0 & 0 \\ 0 & \sigma_P & 0 \\ 0 & 0 & \sigma_P \end{bmatrix} + \begin{bmatrix} -t/3 & 0 & 0 \\ 0 & -t/3 & 0 \\ 0 & 0 & 2t/3 \end{bmatrix}, \qquad \text{(S1)}$$

where σ_P is the hydrostatic stress and *t* is the uniaxial stress component $(\sigma_{33} - \sigma_{11})$.

When deviatoric stress is applied to the material, the measured interplanar d-spacing, $d_m(hkl)$, varies with the angle ψ between+n the diffraction vector and the compression direction. The relationship between $d_m(hkl)$ and the lattice stain, represented by the Q factor $Q(hkl)$ is given by Singh et al. (1998):

$$d_m(hkl) = d_p(hkl)[1 + (1 - 3cos^2\psi)Q(hkl)], \qquad \text{(S2)}$$

where $d_p(hkl)$ is the d-spacing under hydrostatic σ_P. Under hydrostatic stress, $Q(hkl)$ is 0, but as deviatoric stress increases, $d_m(hkl)$, deviates from $d_p(hkl)$ leading to an increase in lattice strain.

The confining pressures for both olivine and antigorite were determined using unit cell volumes calculated from $d_p(hkl)$ and a third order Birch-Murnaghan equation of state (Birch, 1947):

$$P(V) = \frac{3}{2}K_0\left[\left(\frac{V_0}{V}\right)^{\frac{7}{3}} - \left(\frac{V_0}{V}\right)^{\frac{5}{3}}\right] \times \left\{1 + \frac{3}{4}(K_0' - 4)\left[\left(\frac{V_0}{V}\right)^{\frac{2}{3}} - 1\right]\right\}, \qquad \text{(S3)}$$

where V is the measured unit cell volume, V_0, K_0, and K_0' are the unit cell volume, bulk modulus, and pressure derivative of the bulk modulus at ambient conditions, respectively. For olivine, we used the EOS parameters from Zhang and Bass (2016), while for antigorite, we adopted the EOS parameters derived by Bezacier et al., (2013).

Supplementary Text S3: EVPSC Modeling

Elasto-Visco-Plastic Self-Consistent (EVPSC) modeling (Wang et al., 2010) is an effective medium self-consistent approach for linking the activity of slip systems to observed lattice strains. It can produce model textures and macroscopic stress. Like other self-consistent methods, such as Visco-Plastic Self-Consistent (VPSC) model (Lebensohn and Tomé, 1994) and Elasto-Plastic Self-Consistent (EPSC) model (Turner and Tomé, 1994), the EVPSC model treats each grain as an inclusion in a homogenous anisotropic matrix with averaged polycrystal properties, but allows a continuous elasto-plastic transition. As deformation progresses, the inclusion and matrix interact and the macroscopic elasto-plastic properties are updated iteratively until the average strain and stress match the macroscopic values.

In EVPSC models, the rate-sensitive constitutive law that governs the plastic behavior of the inclusions is

$$\dot{\varepsilon}_{ij} = \dot{\gamma}_0 \sum\nolimits_s m^s_{ij} \left\{\frac{m^s_{kl}\sigma_{kl}}{\tau^s}\right\}^n, \qquad \text{(S4)}$$

where $\dot{\varepsilon}_{ij}$ is the strain rate, $\dot{\gamma}_0$ is the reference shear strain rate, m^s_{kl} is the symmetric Schmid factor for the slip system s, σ_{kl} is the local stress tensor, τ^s is the rate sensitive critical resolved shear stress (CRSS) of the slip system s, and n is the stress exponent. The model selects active deformation mode based on the CRSS value and incrementally distribute the stress to each iterative grain accordingly.

The evolution of each plastic deformation mechanism on the slip planes is described using an empirical Voce hardening law (Tomé et al., 1984)

$$\tau^s = \tau^s_0 + (\tau^s_1 + \theta^s_1 \Gamma) \cdot \left(1 - \exp\left[-\frac{\theta^s_0 \Gamma}{\tau^s_1}\right]\right), \qquad \text{(S5)}$$

where $\Gamma$is the accumulated shear in the grain, τ_0^s is the initial CRSS, and θ_0^s and θ_1^s are the initial and asymptotic hardening rates, respectively.

Although EVPSC code allows multi-phase modeling, we only modeled olivine since only the (001) and (102) lattice reflections were processable for antigorite, leaving us with an incomplete picture of the strained unit cell, making EVPSC not useful for evaluating the mechanical properties of the monoclinic antigorite. In contrast, olivine has sufficient number of strong lattice reflections, enabling successful matching of Q-factors to slip systems.

Since this is a two-phase system with likely uneven strain partitioning, the macroscopic strain rate listed in Table 1 are not directly applicable to EVPSC modeling of olivine. Instead, we evaluated strain partitioning between the two phases using SEM images to track relative aspect ratio changes in grains before and after deformation (Fig. 4). Olivine's (021), (101), (002), and (130) reflections were selected for modeling, with input parameters listed in Table 2. Following Burnley et al., (2015), we incorporated seven commonly observed slip systems in olivine along with three unidirectional slip systems representative of kink bands. Our best stress fit was achieved with the tangent homogenization scheme, which accommodates more heterogenous strain from grain to grain and tends to predict a uniform stress state (Castelnau et al., 2008). The model incorporated 3000 crystals with initial textural orientations, with reference elastic moduli for olivine taken from Zhang and Bass, (2016) at corresponding beginning pressures.

Deformation evolution was tracked utilizing the measured macroscopic axial strain and hydrostatic stress. The deformation matrix used in EVPSC was defined based on volume change with increasing axial strain for each strain rate step during the simulation (Fig. S3)

Note, minor textures developed during the process sintering of the two-phase mixtures before deformation. Olivine exhibited very weak alignment of (010) or (001) planes, while antigorite's basal planes compacted perpendicular to the cylinder's long axis, forming a distinct (001) texture. Olivine lattice strains followed the hierarchy $Q(101) < Q(002) < Q(130) \cong Q(021)$. Uncertainties in Q-values were ±0.0005 for (101), (130), and (021) planes, increased to ±0.001 for $Q(002)$ due to weaker diffraction intensity. Q values of Antigorite exhibited larger uncertainties (±0.002), likely owing to peak broadening from its strong texture. For Atg70/Ol30, compression to ~2.5 GPa (D2608) and ~6.7 GPa (D2609) preserved the Q-factor order $Q(101) < Q(002) < Q(021) < Q(130)$, though $Q(002)$ strain in D2609 was ~0.0005 higher (Fig. S4). Dominant slip systems included {011}[100] (pencil glide) and (010)[001] (B-type slip), with significant kinking observed in both runs. Atg50/Ol50 samples compressed to ~3.7 GPa (D2647) and ~7.0 GPa (D2646) showed similar Q-hierarchies ($Q(101) < Q(002) < Q(021) < Q(130)$) in D2647, but $Q(021)$ and $Q(130)$ magnitudes became comparable in run D2646 (Fig. S5). Slip systems remained consistent with that of sample Atg70/Ol30. Samples Atg20/Ol80 (~3.5 GPa in D2703; ~6.4 GPa in D2705) exhibited a modified order of $Q(101) < Q(002) < Q(130) < Q(021)$ (Fig. S6), alongside enhanced activity of the {110}[001] slip system, particularly in D2705. A rotated Atg50/Ol50 sample (D2708) compressed to ~7.6 GPa maintained the Q-hierarchy $Q(101) < Q(002) < Q(130) < Q(021)$. However, strain differences between sequential planes—especially from $Q(101)$ to $Q(021)$—were significantly larger than in all other runs (Fig. S7).

Sample			Atg70/Ol30		Atg50/Ol50		Atg20/Ol80		Atg50/Ol50 with preexisting texture
Experimental run			D2608	D2609	D2646	D2647	D2705	D2703	D2708
Pressure (GPa)			6.77	2.56	7.09	3.78	6.44	3.54	7.67
XRD	Antigorite	M-index	0.0119	0.0107	0.0175	0.0203	0.0016	0.0012	0.0017
		J-index	1.5436	1.5643	1.8394	1.8273	1.0882	1.0587	1.0897
	Olivine	M-index	0.0267	0.0402	0.0365	0.0285	0.0247	0.0112	0.0221
		J-index	2.0596	3.0008	2.1789	2.015	1.6974	1.1884	1.5783
EBSD	Antigorite	M-index	0.2352		0.2698				
		J-index	5.9547		15.0622				
	Olivine	M-index	0.1773		0.1536				
		J-index	4.5648		4.1409				

Table S1. M- and J-index of the sample’s fabrics obtained from the in-situ XRD experiment and ex-situ EBSD measurements, respectively.

References	Pressure (Gpa)	Temperature (K)	Strain rate (*$10^{-5}s^{-1}$)
This study HP	6.44 - 7.09	673	2.77 - 4.66
This study LP	2.56 - 3.78	673	3.27 - 5.16
Hilairet et al. (2007)	1.0 - 4.0	473 - 773	0.1 - 10
Chernak and Hirth (2010)	0.85 - 1.5	573 - 898	~1.5
Protor and Hirth (2016)	1.0 - 2.0	573 - 773	~2.3
Hirauchi et al. (2020)	1.0 - 2.5	573 - 873	~1.5
Shao et al. (2021)	1.1 - 1.5	673 - 873	0.1 - 119
Hilairet et al. (2024)	2.0 - 5.0	623	1.58 - 4.52

Table S2. The pressures, temperatures, and strain rates of all experimental runs in this study and previous studies.

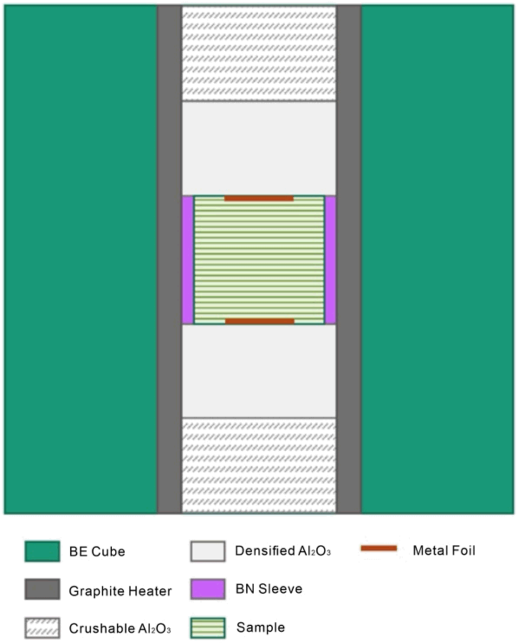

Fig. S1. Schematic cross-section of the D-DIA sample assembly. The Ni or Au metal foil is ~0.1 µm thick. The horizontal stripes in the sample indicate the weak alignment of the antigorite's basal plane in the starting samples for all experimental runs except D2708. The vertical direction is the compressional direction Z.

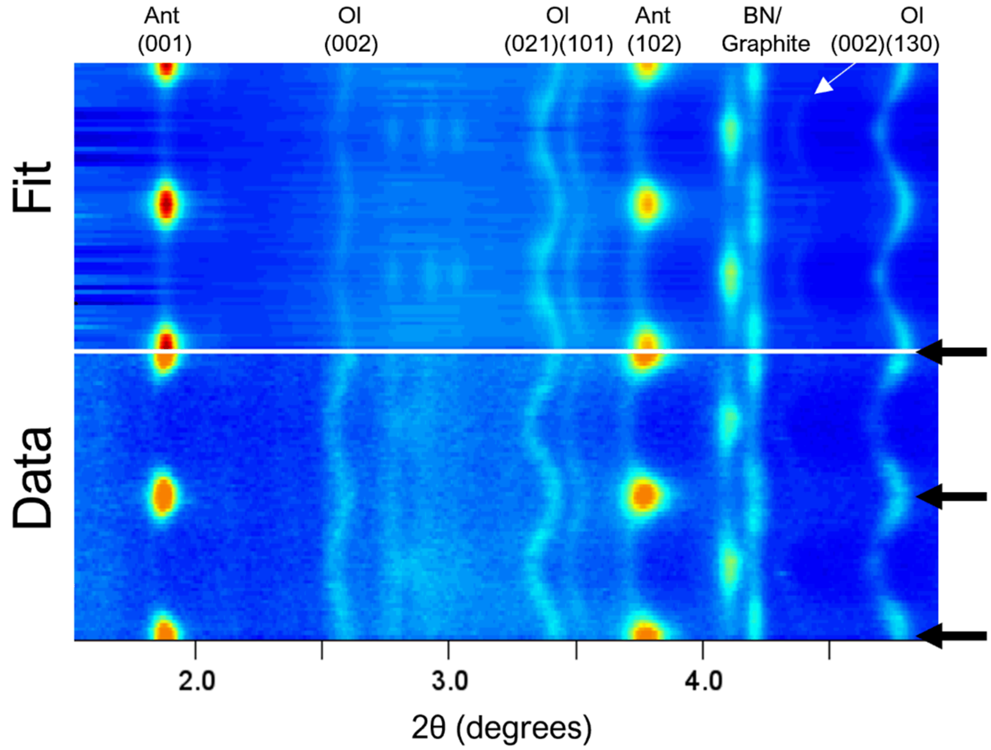

Fig. S2. A typical unrolled diffraction image and MAUD fit of experiment D2647 at ~11% strain. Systematic intensity variations along the azimuth indicate texture of corresponding mineral phases, whereas sinusoidal variations reflect lattice strain.

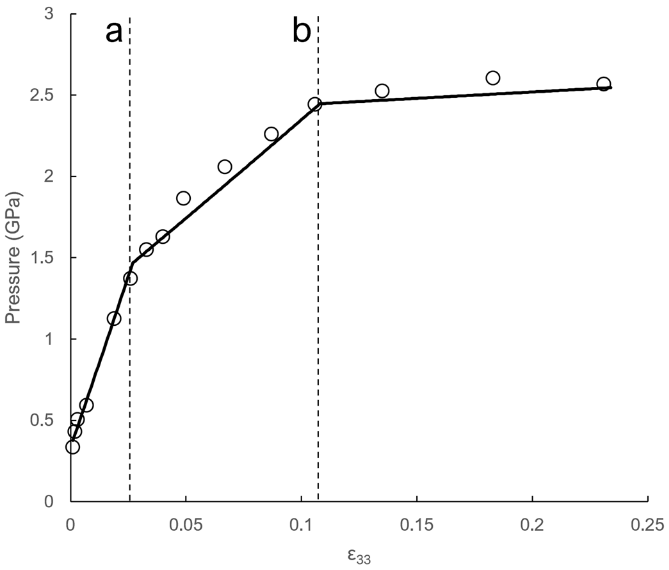

Fig. S3. Pressure versus axial strain ε_{33} of olivine in run D2609. Experimental data are shown in circles and EVPSC simulation results are shown in solid line. Dashed line **a** represents the increase in strain rate from $7.42*10^{-6}$ s^{-1} to $2.98*10^{-5}$ s^{-1} and dashed line **b** represents the increase in strain rate from $2.98*10^{-5}$ s^{-1} to $1.18*10^{-4}$ s^{-1}.

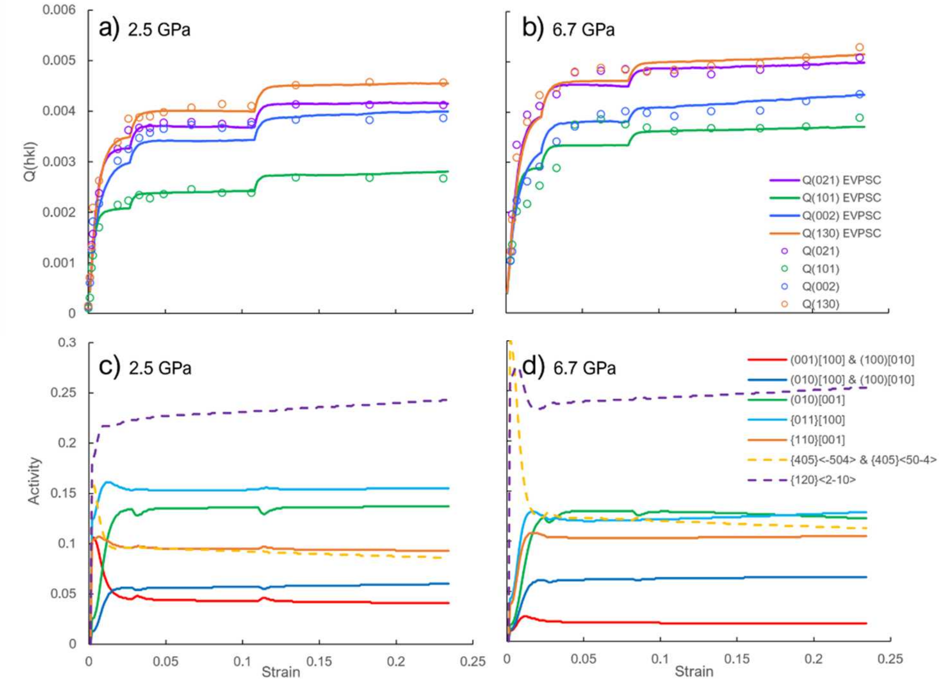

Fig. S4. EVPSC simulation results: (a) and (b) Experimental and modeled Q(hkl) of olivine in experimental run D2609 and D2608, respectively. (c) and (d) show slip system activity of olivine, with dashed lines indicating kink-band systems.

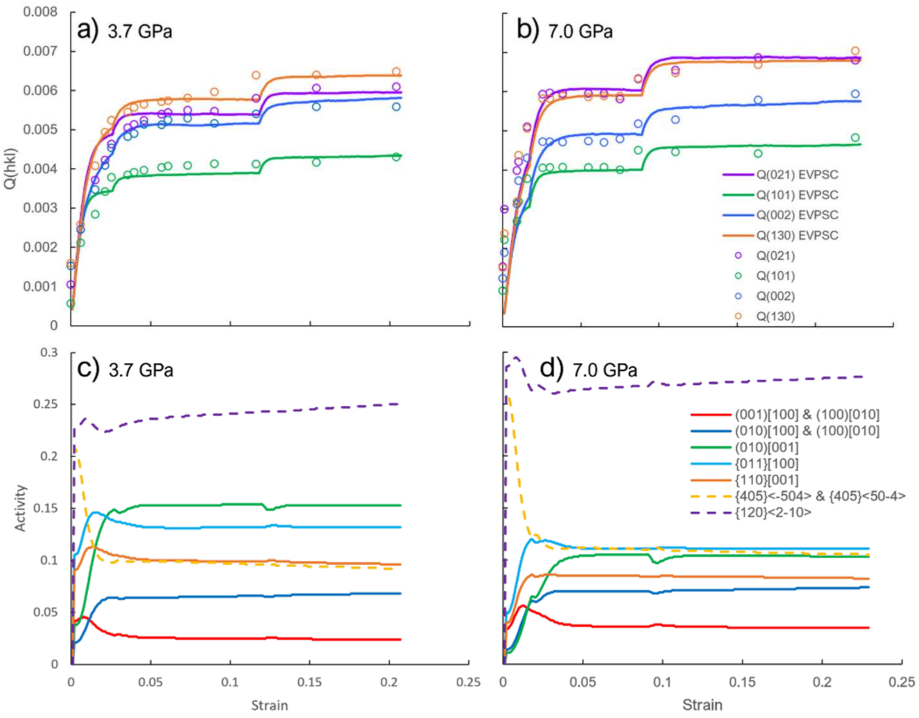

Fig. S5. EVPSC simulation results: (a) and (b) Experimental and modeled Q(hkl) of olivine in experimental runs D2647 and D2646, respectively. (c) and(d) show slip system activity of olivine with dashed lines indicating kink-band systems.

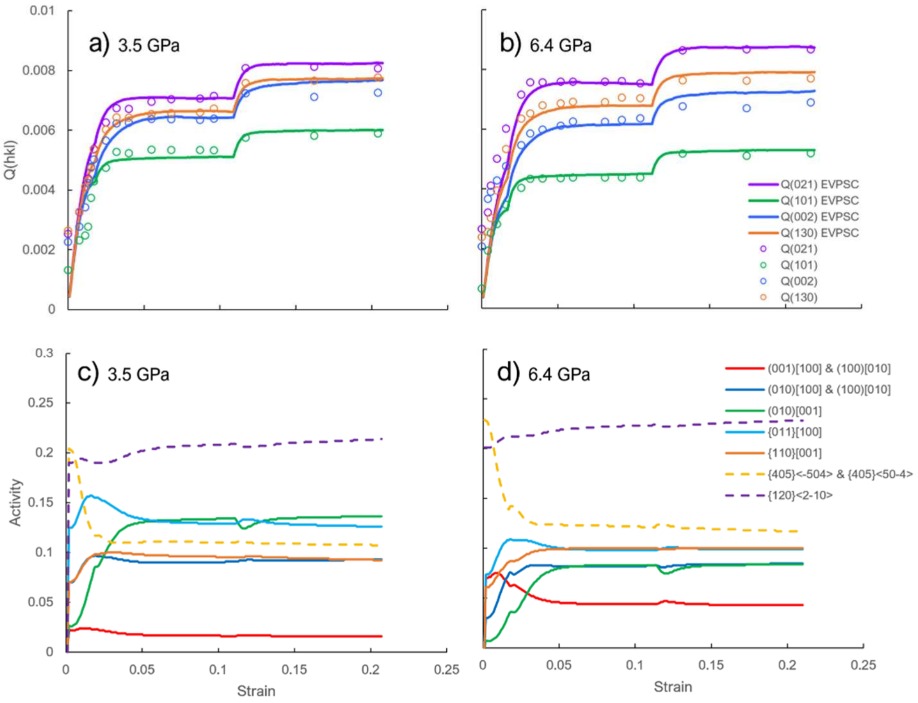

Fig. S6. EVPSC simulation results: (a) and (b) Experimental and modeled Q(hkl) of olivine in experimental runs D2703 and D2705, respectively. (c) and (d) show slip system activity of olivine with dashed lines indicating kink-band systems.

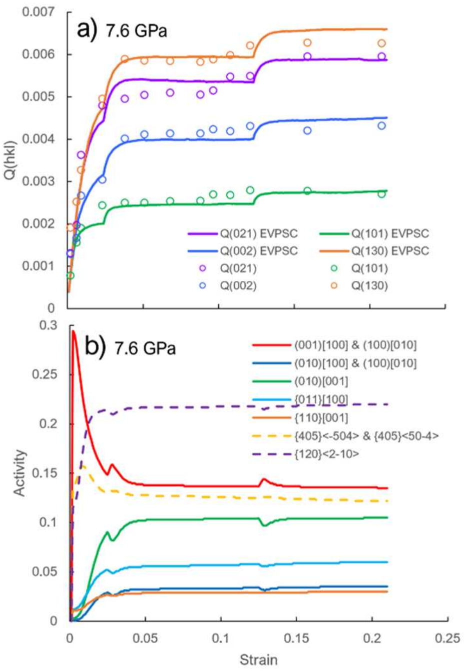

Fig.S7. EVPSC simulation results: (a) Experimental and modeled Q(hkl) of olivine in experimental run D2708. (b) show slip system activity of olivine with dashed lines indicating kink-band systems.

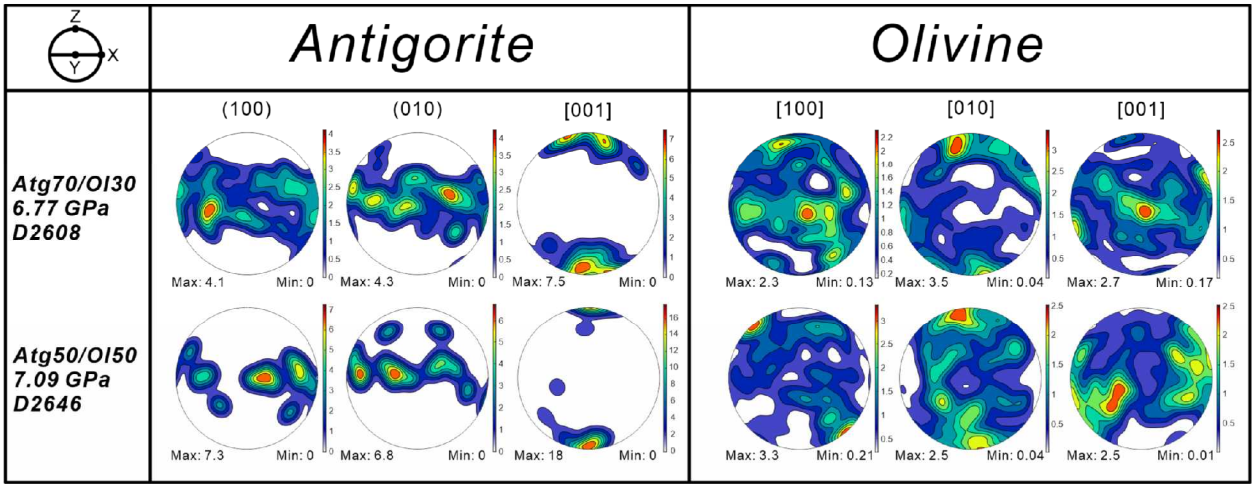

Fig. S8. CPO of antigorite and olivine in the recovered samples measured by EBSD. It is well-known that obtaining usable EBSD measurements of deformed antigorite crystals is extremely challenging, thus, the numbers of usable EBSD data points for antigorite are only 44 and 13 in experimental run products of D2646 and D2608, compared to 102 and 146 for olivine, respectively.

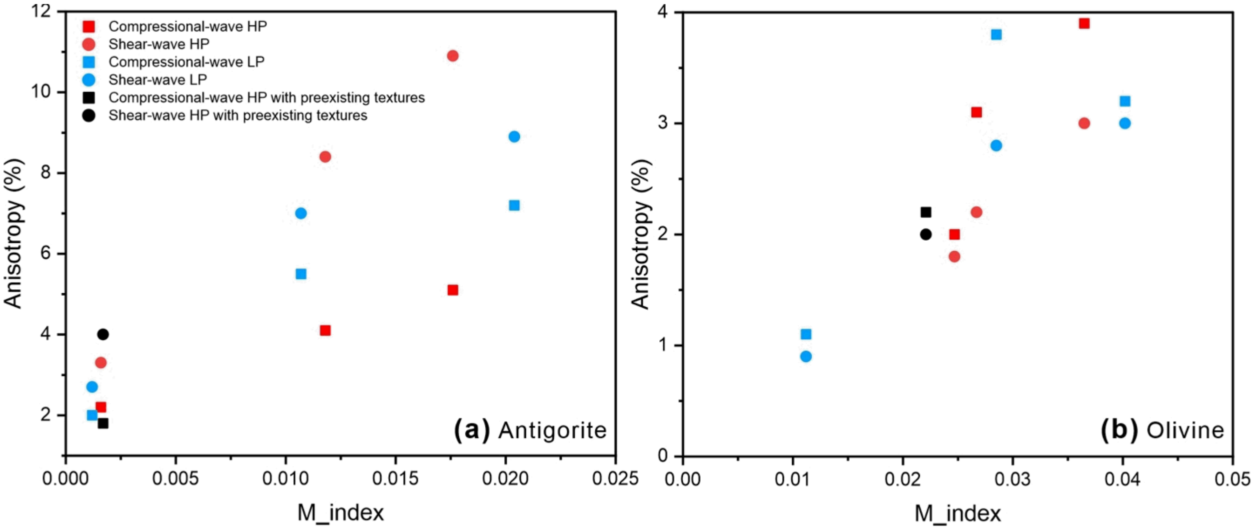

Fig. S9. Change of shear-wave anisotropy of (a) antigorite and (b) olivine as a function of M-index.

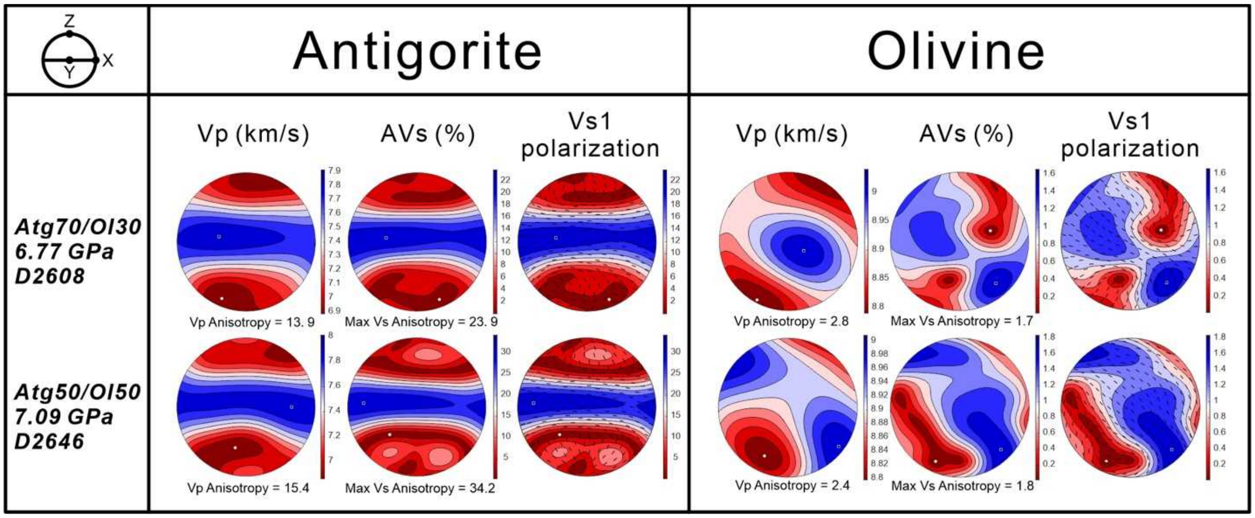

Fig. S10. Calculated acoustic anisotropy for antigorite and olivine in different experimental runs based on EBSD measurements.

References:

Bachmann, F., Hielscher, R., Schaeben, H., 2010. Texture Analysis with MTEX – Free and Open Source Software Toolbox. Solid State Phenomena 160, 63–68. https://doi.org/10.4028/www.scientific.net/ssp.160.63

Bezacier, L., Reynard, B., Cardon, H., Montagnac, G., Bass, J.D., 2013. High-pressure elasticity of serpentine and seismic properties of the hydrated mantle wedge. J. Geophys. Res.: Solid Earth 118, 527–535. https://doi.org/10.1002/jgrb.50076

Burnley, P., 2015. Elastic plastic self-consistent (EPSC) modeling of plastic deformation in fayalite olivine. American Mineralogist Special Collection: Olivine 100, 1424-1433. http://dx.doi.org/10.2138/am-2015-5234CCBYNCND

Birch, F., 1947. Finite elastic strain of cubic crystals. Phy. Rev. 71(11), 809

Capitani G, Mellini M. 2004. The modulated crystal structure of antigorite: The m = 17 polysome. American Mineralogist, 89, 147-158.

Castelnau, O., Blackman, D. K., Lebensohn, R., Ponte Castaneda, P., (2008). Micromechanical modeling for the Viscoplastic behavior of olivine. . J. Geophys. Res.: Solid Earth, 113 (B9), https://doi.org/10.1029/2007JB005444

Lebensohn, R., & Tomé, C. N., 1994. A self-consistent viscoplastic model: prediction of rolling textures of anisotropic polycrystals. Materials Science and Engineering: A, 175(1-2), 71-82.

Singh, A. K., C. Balasingh, H. K. Mao, R. J. Hemley, and J. F. Shu., 1998. Analysis of lattice strains measured under nonhydrostatic pressure, J. Appl. Phys., 83(12), 7567–7575, doi:10.1063/1.367872

Smyth J R, Hazen R M. 1973. The crystal structures of forsterite and hortonolite at several temperatures up to 900 ºC. American Mineralogist 58, 588-593

Turner, P. A., & Tomé, C. N., 1994. A study of residual stresses in Zircaloy-2 with rod texture. Acta metallurgica et Materialia, 42(12), 4143-4153.

Wang, H., Wu, P.D., Tomé, C.N., Huang, Y., 2010. A finite strain elastic–viscoplastic self-consistent model for polycrystalline materials. Journal of the Mechanics and Physics of Solids 58(4), b594-612, https://doi.org/10.1016/j.jmps.2010.01.004

Zhang, J.S., Bass, J.D., 2016. Sound velocities of olivine at high pressures and temperatures and the composition of Earth's upper mantle. Geophys. Res. Lett. 43, 9611–9618. https://doi.org/10.1002/2016gl069949